SANDIA REPORT
SAND2016-11186
Unlimited Release
Printed November 2016

Fully-Coupled Thermo-Electrical Modeling and Simulation of Transition Metal Oxide Memristors

Denis Mamaluy, Xujiao Gao, Harold Hjalmarson, Matthew Marinella,
Patrick Mickel, Brian D. Tierney

Prepared by
Sandia National Laboratories
Albuquerque, New Mexico 87185 and Livermore, California 94550

Sandia National Laboratories is a multi-mission laboratory managed and operated by Sandia Corporation, a wholly owned subsidiary of Lockheed Martin Corporation, for the U.S. Department of Energy's National Nuclear Security Administration under contract DE-AC04-94AL85000.

Issued by Sandia National Laboratories, operated for the United States Department of Energy by Sandia Corporation.

Available to DOE and DOE contractors from
U.S. Department of Energy
Office of Scientific and Technical Information
P.O. Box 62
Oak Ridge, TN 37831

Telephone: (865) 576-8401
Facsimile: (865) 576-5728
E-Mail: reports@osti.gov
Online ordering: http://www.osti.gov/scitech

Available to the public from
U.S. Department of Commerce
National Technical Information Service
5301 Shawnee Rd
Alexandria, VA 22312

Telephone: (800) 553-6847
Facsimile: (703) 605-6900
E-Mail: orders@ntis.gov
Online order: http://www.ntis.gov/search

SAND2016-11186
Unlimited Release
Printed November 2016

FULLY-COUPLED THERMO-ELECTRICAL MODELING AND SIMULATION OF TRANSITION METAL OXIDE MEMRISTORS

Denis Mamaluy, Xujiao Gao, Harold Hjalmarson,
Matthew Marinella, Patrick Mickel, Brian D. Tierney
Sandia National Laboratories
P.O. Box 5800
Albuquerque, New Mexico 87185-MS1322

Abstract

Transition metal oxide (TMO) memristors have recently attracted special attention from the semiconductor industry and academia. Memristors are one of the strongest candidates to replace flash memory, and possibly DRAM and SRAM in the near future. Moreover, memristors have a high potential to enable beyond-CMOS technology advances in novel architectures for high performance computing (HPC). The utility of memristors has been demonstrated in reprogrammable logic (cross-bar switches), brain-inspired computing and in non-CMOS complementary logic. Indeed, the potential use of memristors as *logic devices* is especially important considering the inevitable end of CMOS technology scaling that is anticipated by 2025. In order to aid the on-going Sandia memristor fabrication effort with a memristor design tool and establish a clear physical picture of resistance switching in TMO memristors, we have created and validated with experimental data a simulation tool we name the Memristor Charge Transport (MCT) Simulator.

ACKNOWLEDGMENTS

This work was funded at Sandia National Laboratories under the LDRD Project #173024 and Title "Simulation Capability and Computational Assessment of Memristors as Beyond-CMOS Logic and Memory Devices". Sandia National Laboratories is a multiprogram laboratory operated by Sandia Corporation, a Lockheed Martin Company, for the United States Department of Energy's National Nuclear Security Administration under Contract DE-AC04-94AL85000.

CONTENTS

FIGURES

TABLES

NOMENCLATURE

TCAD	Technology Computer Aided Design
TMO	Transition Metal Oxide
MCT	Memristor Charge Transport
Charon	Charon Device Simulator (TCAD tool)
TaOx	Tantalum Oxide
CMOS	complementary metal–oxide–semiconductor
PDE	Partial Differential Equation
BC	Boundary Conditions
FE	Finite Element
SUPG	Streamline Upwind Petrov Galerkin
EFFG	Exponentially Fitted Flux Galerkin
CF	Conducting Filament
NEGF	Non-equilibrium Green's function
HPC	High Performance Computing
DOE	Department of Energy
SNL	Sandia National Laboratories
ITRS	International Technology Roadmap for Semiconductors

1. INTRODUCTION

1.1. The Need for a Comprehensive Predictive Memristor Simulator

Transition metal oxide (TMO) memristors have recently attracted special attention from the semiconductor industry and academia. Memristors are one of the strongest candidates to replace flash memory, and possibly DRAM and SRAM in the nearest future [1,2]. Moreover, memristors have a high potential to enable beyond-CMOS technology advances in novel architectures for high performance computing (HPC). The utility of memristors has been demonstrated in reprogrammable logic (cross-bar switches [3,4]), brain-inspired computing [5] and in non-CMOS complementary logic [6]. This potential use of memristors as *logic devices* is especially important considering the inevitable end of CMOS technology scaling that is anticipated to occur by 2025. However, despite the spectacular progress in experimental demonstration and fabrication of TMO memristors, their microscopic transport theory and even some key operational principles, essential to advance experimental progress, remain uncertain [7,8,9,10]. In order to establish a clear physical picture of resistance switching in TMO memristors and to aid in the on-going Sandia memristor fabrication efforts, we have created and validated with experimental data a simulation tool we name the Memristor Charge Transport (MCT) Simulator.

The concept of a *memristor* was proposed by Leon Chua [11] in 1971 from pure symmetry arguments. Resistive memory effects, i.e., hysteretic current-voltage (I-V) behavior, have been experimentally observed in thin film metal oxides since the 1960s [12]. However, the connection between the observed I-V hysteresis and Chua's memristor concept was not established until 2008 when researchers from HP Labs [13] demonstrated that many nanoscale electronic devices, including thin film metal oxides that exhibited hysteretic I-V switching, are in fact memristors and that *memristance* arises naturally in nanoscale systems in which solid-state electronic and ionic transport are coupled under the influence of an external bias voltage. In recent years, progress in developing memristive devices (especially TMO-based) has quickly advanced to the point where they may soon be useful for beyond-CMOS memory and logic applications [1-4]. Concurrently, an understanding of the underlying physical switching mechanisms has also been improving [14,15,16]. However, these mechanisms are still far from being understood, and this imposes a significant barrier to the development and application of memristors [16].

Memristive switching phenomena, observed in numerous oxides and memristive devices, can be categorized in many different ways [14,15]. We adopt the classification convention defined in [16], i.e., anion and cation devices, and thus focus on the anion-based devices for this work, as they are most relevant to beyond-CMOS applications. In anion devices, oxygen anions (or positively charged oxygen vacancies) are thought to be mobile species, in addition to electrons and holes. Examples of such devices include TiO_x [17,18], TaO_x [19], NiO_x [20] memristors. The switching mode of these devices can be bipolar or unipolar, depending primarily on the material and structure of the device, and the interplay between electrical and thermal effects. The relative importance of electric field drift and Joule heating leads to four main switching modes: bipolar nonlinear, bipolar linear, nonpolar bistable, and nonpolar threshold switching, as schematically shown in Figure 1 (a-d) (taken from [16]). It has been proposed [14-16] that four main driving forces are responsible for the different switching behavior: electric potential gradient (field drift), electron kinetic energy (electromigration), species concentration gradient (Fickian diffusion), and temperature gradient (thermophoresis, or the Soret effect). These driving forces may work independently or together to produce the switching types in Figure 1 (a-d). However, the microscopic picture of how exactly these factors drive the mobile species to generate a particular type of switching is still under debate.

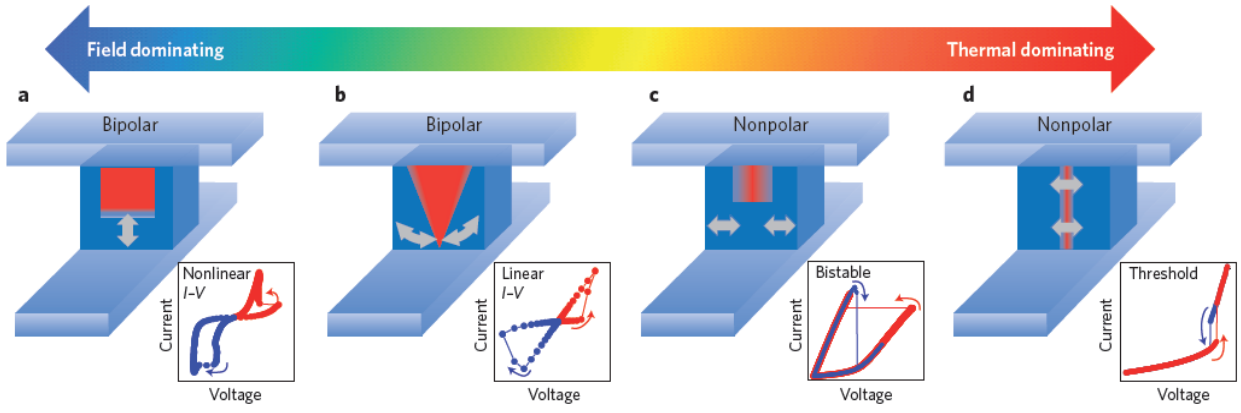

Figure 1. Schematics of conduction channels (red) in switching matrix materials (blue) in four typical switching devices, where both electric field and Joule heating drive the switching. The grey arrows indicate the idealized ionic motion. The inset to each schematic shows typical switching current–voltage curve.

There has been significant modeling effort [21,22,23,24,25,26,27,28,29] to facilitate the understanding of switching physics in memristive devices. One branch of analysis focused on extracting proper expressions for state variables on a circuit level by carefully fitting experimental data [21,22]. While useful in particular applications, this approach cannot aid in the understanding of microscopic switching mechanisms and general device modeling. Another branch of the effort focused on providing a model based on numerical solutions of one-dimensional (1D) coupled drift-diffusion equations for electrons, holes, and ions [23]. Although this model provided certain insight into the switching dynamics, it neglected the very important thermal effects and oversimplified the treatment of electron transport. Furthermore, modeling of Joule heating effects has been either limited to analytic compact models [24,25], extracted from fitting experimental data, or steady-state heat flow simulation for given heat source [26]. In other work, an electro-thermal simulation was performed in an attempt to take into account both electrical and thermal effects simultaneously [27,28]. However, the treatment of electrical conduction was overly simplistic, with the underlying assumption that the device is a "metal" with a given temperature-dependent conductivity. In another effort, more physics were included in the electrical transport model by solving a 1D Soret-Fick continuity equation for ions in cylindrical coordinates [29] using a known temperature profile obtained in [25]. However, until now there has been no reported work that treated on an equal footing the electrical transport of electrons, holes, and ions/vacancies, and thermal Joule heating effects.

1.2. Overall Description of the MCT Simulator

We have developed a physics-based continuum model that treats the transport of electrons, holes, and ions/vacancies, together with the Joule heating, on an equal footing for realistic geometries. Namely, we have created a MCT Simulator that solves simultaneously the following coupled differential equations: the time-dependent drift-diffusion equations for electrons, holes, and ions/vacancies, the time-dependent lattice heat equation, and the Poisson equation for all charged species in three spatial dimensions (see the next Section). The drift-diffusion equation for each species includes field drift currents due to electric potential gradients, concentration gradients (Fickian diffusion), and temperature gradients (Soret effect). The heat equation contains Joule heating contributions from all the species.

We have implemented the continuum memristor transport model in the Charon code, which is Sandia's multi-dimensional semiconductor device transport simulator. It is built upon the Trilinos/Panzer toolkit that provides cutting-edge mathematical libraries, discretization utilities, and distributed parallel capability. It solves the drift-diffusion equations for electrons and holes in semiconductor devices [30]. The code is naturally applicable to 1D/2D/3D devices with distributed parallel capability. This allowed us to simulate real, 3D memristive devices.

During the development of the MCT Simulator, we faced a number of challenges. Firstly, the specific combination of charge transport and switching mechanisms in TMO memristors were still a subject of debate during this time [21-29]. Secondly, material properties in TaOx materials were not well known and could vary significantly from device to device due to process variation. To mitigate these challenges, we leveraged knowledge gained from the NTM LDRD and HP CRADA, as well as other published papers, to identify the proper physical models for electrical mobility, diffusion, and Soret coefficients, and to calibrate necessary parameters. We have implemented new physical effects and models which have allowed us to accurately simulate resistive switching effects in TaOx memristors and obtain the corresponding electrical characteristics. In particular, we did the following:

- Augmented Charon with the fully-coupled electrical transport equations for different charge carrier species.
- Added Soret effects and thermal transport equations for self-heating analysis.
- Performed identification and calibration of sophisticated physical models and materials parameters for TaOx devices.
- Identified criteria of importance of chemical reactions in memristive switching and studied numerous transport mechanisms in TaOx materials.
- Successfully validated the MCT Simulator on the existing experimental data.
- Created a design tool that allows accurate prediction of memristor electrical characteristics.

In the following sections, we discuss the details of the implementation and validation of the multiple-charge species transport equations and the Soret/self-heating effects. In doing so, we will explain the material models used to simulate switching in TaOx memristors, and will demonstrate the very good agreement between our simulated results and experimental data.

2. FULLY-COUPLED THERMO-ELECTRICAL TRANSPORT MODEL

In this section, we present the details of the fully-coupled thermo-electrical transport model implemented in the Charon TCAD tool as the MCT Simulator.

2.1. Transport Equations

Our fully-coupled electrical and thermal transport model includes all of the most important processes that govern the switching dynamics of oxide-based memristors and treats the transport of electrons, holes, and vacancies together with Joule heating on an equal footing. Namely, we solve simultaneously the five coupled partial differential equations (PDEs):

$$\nabla \bullet \varepsilon_0 \varepsilon_r \nabla(\phi - \theta) = -q(p - n + n_V + C) \qquad \backslash^* \text{ MERGEFORMAT (1)}$$

$$\frac{\partial n}{\partial t} = \frac{1}{q}\nabla \bullet \boldsymbol{J}_n - R_{net} \qquad \backslash^* \text{ MERGEFORMAT (2)}$$

$$\frac{\partial p}{\partial t} = -\frac{1}{q}\nabla \bullet \boldsymbol{J}_p - R_{net} \qquad \backslash^* \text{ MERGEFORMAT (3)}$$

$$\frac{\partial n_V}{\partial t} = -\frac{1}{q}\nabla \bullet \boldsymbol{J}_V \qquad \backslash^* \text{ MERGEFORMAT (4)}$$

$$\frac{\partial}{\partial t}\left(c_L T\right) - \nabla \bullet (\kappa_L \nabla T) = H \qquad \backslash^* \text{ MERGEFORMAT (5)}$$

Equations * MERGEFORMAT (2)-* MERGEFORMAT (4) are the time-dependent continuity equations governing the transport of electrons (denoted as n), holes (p), and oxygen vacancies (n_V), respectively. For simplicity, we assume that oxygen vacancies behave as positive, singly charged particles throughout this report. R_{net} represents a net recombination rate due to all possible electron-hole generation / recombination processes, while possible reactions between oxygen vacancies and electrons / holes are neglected. The Poisson equation * MERGEFORMAT (1) captures the electrostatic effects from all charged species, where C represents a net positive charge from fixed dopants, i.e., $C = N_D^+ - N_A^-$, with N_D^+ being fixed donors, and N_A^- fixed acceptors. Note the left hand side of the Poisson equation uses (ϕ-θ) instead of ϕ alone, since ϕ here is chosen to be the intrinsic Fermi potential (i.e., negative of the intrinsic Fermi level), and θ is a band structure parameter and chosen such that (ϕ-θ) represents the

vacuum potential. Specifically, θ is chosen to be the difference between the vacuum energy level and the intrinsic Fermi level, and is given by

$$\theta = \frac{1}{q}\left[\chi + \frac{1}{2}E_g + \frac{1}{2}k_B T \ln\left(\frac{N_C}{N_V}\right)\right] \qquad \text{* MERGEFORMAT (6)}$$

where χ, E_g, N_C, and N_V are the electron affinity, band gap, electron effective density of states, and hole effective density of states, respectively, of the material used. Additonally, T is the lattice temperature, q is the elemental charge, and k_B is the Boltzmann constant. In a homo- or hetero-junction device with a spatially varying temperature, the vacuum potential satisfies the Poisson equation. However, solving the vacuum potential directly from the coupled PDEs often shows numerical convergence problems [31]. Hence a more robust and popular choice is to rewrite the Poisson equation in the form of Eq. * MERGEFORMAT (1) and solve for the intrinsic Fermi potential, an approach also widely used in commercial TCAD codes [32]. Equation * MERGEFORMAT (5) is the time-dependent Fourier heat equation which models the Joule heating effect.

The current densities for electrons, holes, and vacancies include contributions from the field drift due to the potential gradient, Fickian diffusion due to the concentration gradient, and the Soret effect due to the temperature gradient. They are given by Eqs. * MERGEFORMAT (7)-* MERGEFORMAT (9):

$$\boldsymbol{J}_n = qn\mu_n \boldsymbol{F} + qD_n \nabla n + k_B n \mu_n \nabla T \qquad \text{* MERGEFORMAT (7)}$$

$$\boldsymbol{J}_p = qp\mu_p \boldsymbol{F} - qD_p \nabla p - k_B p \mu_p \nabla T \qquad \text{* MERGEFORMAT (8)}$$

$$\boldsymbol{J}_V = qn_V \boldsymbol{v}_V - qD_V \nabla n_V - qD_V S_V n_V \nabla T \qquad \text{* MERGEFORMAT (9)}$$

Where $\boldsymbol{F} = -\nabla\phi$ is the electric field. Equations * MERGEFORMAT (7)-* MERGEFORMAT (8) are the standard drift-diffusion equations including temperature gradient for electrons and holes, and can be derived [33] from the well-known semi-classical Boltzmann transport equation under various assumptions. The electron (hole) mobility is related to the electron (hole) diffusion coefficient through the Einstein relation, i.e., $D_n / \mu_n = D_p / \mu_p = k_B T / q$, for Boltzmann statistics. The three terms in Eq. * MERGEFORMAT (9) for the vacancy current density show the same signs as those of holes in Eq. * MERGEFORMAT (8), which is consistent with the assumption that vacancies and holes are both positively charged. The third term in Eq. * MERGEFORMAT

(9) describes the Soret effect and is taken from Ref. [34]. The models for the vacancy velocity, diffusion and Soret coefficients will be discussed in a later section. It is noted that for electrons and holes, high-doping effects such as band gap narrowing and Fermi-Dirac statistics are also included. When Fermi-Dirac statistics is used, the D/μ relation is modified to include the Fermi-Dirac integrals, i.e., $\frac{D}{\mu}=\frac{k_B T}{q}\frac{F_{1/2}(\eta)}{F_{-1/2}(\eta)}$, where $F_{1/2}(\eta)$ and $F_{-1/2}(\eta)$ are Fermi-Dirac integrals of 1/2 order and -1/2 order respectively.

The heat generation in Eq. * MERGEFORMAT (5) can be modeled with different levels of sophistication [35,36,37,38,39,40]. Because it is generally accepted that Joule heating is the most dominant heat generation source in memristive devices, we model the heat generation as

$$H=\left(\boldsymbol{J}_n+\boldsymbol{J}_p+\boldsymbol{J}_V\right)\bullet\boldsymbol{F}+R_{net}(E_g+3k_BT) \quad \text{* MERGEFORMAT (10)}$$

which includes Joule heating due to all charge carriers and contribution from possible electron-hole recombination processes.

Equations * MERGEFORMAT (4)-* MERGEFORMAT (6), the last (Soret) terms in equations * MERGEFORMAT (7) and * MERGEFORMAT (8), equations * MERGEFORMAT (9) and * MERGEFORMAT (10) have been implemented within the Memristor Simulation LDRD to augment equations * MERGEFORMAT (1)-* MERGEFORMAT (3) that already existed in Charon.

2.2. Rigid Point Ion Model

The velocity of vacancies in memristors is widely modeled using the rigid point ion model [41,42, 43]. However, the original model in Ref. [43] was proposed only for one spatial dimension (1D), and subsequent papers also describe the model in 1D only. To extend the model to multi-dimensional applications, we apply the model in all spatial dimensions. That is, each component i ($i = x, y, z$) of the velocity is given by the rigid point model as

$$v_{V,i}=2fa\exp\left(\frac{-E_a}{k_BT}\right)\sinh\left(\frac{qaF_i}{2k_BT}\right)=\mu_V F_c\sinh(F_i/F_c),\ \text{where } i=x,y,z \quad \text{* MERGEFORMAT (11)}$$

Where f is the frequency of escape attempts, often in the range of 10^{12} -10^{13} Hz, and a is the periodicity of lattice sites, in the range of a few Angstroms, while E_a is the activation energy representing the energy barrier for ions/vacancies to surmount and its value varies significantly in literature. Additionally, F_i is the ith component of electric field, F_c denotes the critical field and

is equal to $F_c = 2k_BT/(qa)$, and μ_V denotes the ion mobility which is given by Eq. * MERGEFORMAT (12). The vacancy diffusion coefficient is computed using Eq. * MERGEFORMAT (13).

$$\mu_V = \frac{qfa^2}{k_BT}\exp\left(\frac{-E_a}{k_BT}\right) \qquad \text{* MERGEFORMAT (12)}$$

$$D_V = \frac{k_BT}{q}\mu_V = fa^2\exp\left(\frac{-E_a}{k_BT}\right) \qquad \text{* MERGEFORMAT (13)}$$

It is clear from Eq. * MERGEFORMAT (11) that the vacancy velocity shows a very strong dependence on temperature and electric field. Figure 2 shows the vacancy velocity in 1D as a function of electric field at temperatures of 300 K to 1000 K in 100 K intervals for a given set of parameters where $f = 10^{12}$ Hz, $a = 0.1$ nm, $E_a = 0.8$ eV. It is seen that for temperatures in the 300 K to 600 K range, an increase of 100 K in temperature leads to an increase of vacancy velocity by several orders of magnitude, while for higher temperatures, the increase of vacancy velocity with temperature significantly less pronounced. On the other hand, the vacancy velocity increases linearly with electric field until the field exceeds a critical value, beyond which the velocity increases exponentially with field.

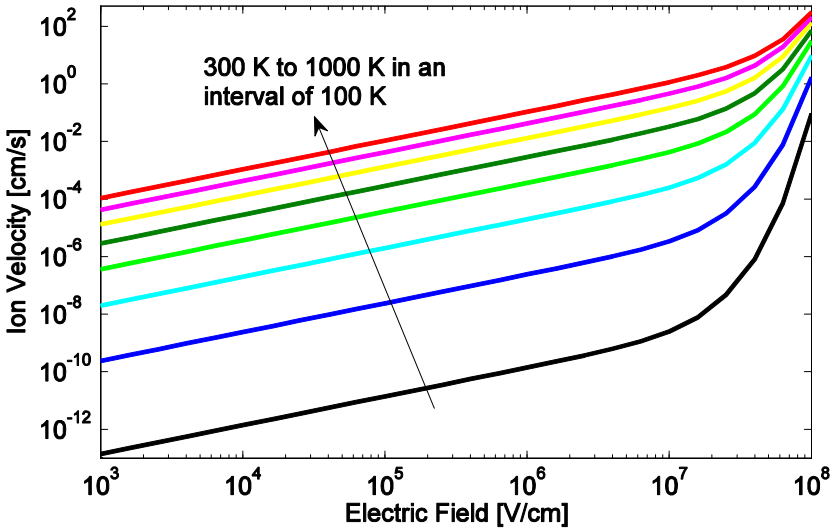

Figure 2. Vacancy velocity dependence on electric field and temperature for a given set of parameters where $f = 10^{12}$ Hz, $a = 0.1$ nm, $E_a = 0.8$ eV.

It is seen that with the rigid point ion model the vacancy diffusion coefficient has an Arrhenius dependence on the temperature. During simulation, in order to prevent an unphysical piling-up of vacancies, the vacancy diffusion coefficient used in the Fickian diffusion term is artificially increased as a function of increasing vacancy density according to $D_V = D_{V,RPI} / (1-n_V/n_{V,max})$, where $D_{V,RPI}$ is determined by the RPI model [i.e., by Eq. * MERGEFORMAT (13)], n_V is the vacancy density, and $n_{V,max}$ represents the maximum allowed oxygen vacancy density. A similar approach was used in Ref. [44] to avoid an unphysically large vacancy density.

2.3. Boundary Conditions

The boundary conditions (BCs) for electric potential, electron density, and hole density are of two types: homogenous Neumann and Ohmic. All non-Ohmic boundaries satisfy the homogenous Neumann condition, i.e., $\nabla\phi \bullet \hat{\eta} = \boldsymbol{J}_n \bullet \hat{\eta} = \boldsymbol{J}_p \bullet \hat{\eta} = 0$, where $\hat{\eta}$ denotes the outer normal of a boundary. Ohmic BCs are determined by charge neutrality and thermal equilibrium conditions. Both Fermi-Dirac and Maxwell-Boltzmann statistics are considered in determining the Ohmic BCs. However, for simplicity, the following description assumes Boltzmann statistics. Namely, at Ohmic boundaries, we have

$$p_0 - n_0 + n_V + C = 0 \qquad \text{* MERGEFORMAT (14)}$$

$$n_0 p_0 = n_{ie}^2 \qquad \text{* MERGEFORMAT (15)}$$

Where V_a is the applied voltage. The equilibrium electron and hole densities are given by

$$n_0 = N_C \exp\left(\frac{E_F - E_C}{k_B T}\right) \qquad \text{* MERGEFORMAT (16)}$$

$$p_0 = N_V \exp\left(\frac{E_V - E_F}{k_B T}\right) \qquad \text{* MERGEFORMAT (17)}$$

The conduction and valence band edges are related to the electric potential through the following expressions: $E_C = E_{vac} - \chi = q\theta - q\varphi - \chi$ and $E_V = E_C - E_g$. Using these relations and Eqs. * MERGEFORMAT (14) -* MERGEFORMAT (17), we can obtain the carrier densities and electric potential at Ohmic boundaries. Specifically, for n-type material, we have

$$n_0 = \frac{N_{eff}}{2} + \sqrt{\left(\frac{N_{eff}}{2}\right)^2 + n_{ie}^2}, \quad \text{where } N_{eff} = C + n_V \quad \backslash^* \text{ MERGEFORMAT (18)}$$

$$p_0 = \frac{n_{ie}^2}{n_0}, \quad \text{where } n_{ie} = \sqrt{N_C N_V}\exp\left(\frac{-E_g}{2k_B T}\right) \quad \backslash^* \text{ MERGEFORMAT (19)}$$

$$\phi = \frac{1}{q}\left(q\theta - \chi\right) + \frac{k_B T}{q}\ln\left(y\right) + V_a, \; y = \frac{N_{eff}}{2N_C} + \left[\left(\frac{N_{eff}}{2N_C}\right)^2 + \frac{N_V}{N_C}\exp\left(\frac{-E_g}{k_B T}\right)\right]^{1/2} \quad \backslash^* \text{ MERGEFORMAT (20)}$$

For p-type material, the corresponding expressions are

$$n_0 = \frac{n_{ie}^2}{p_0}, \; n_{ie} = \sqrt{N_C N_V}\exp\left(\frac{-E_g}{2k_B T}\right) \qquad \backslash^* \text{ MERGEFORMAT (21)}$$

$$p_0 = \frac{-N_{eff}}{2} + \sqrt{\left(\frac{N_{eff}}{2}\right)^2 + n_{ie}^2}, \; N_{eff} = C + n_V \quad \backslash^* \text{ MERGEFORMAT (22)}$$

$$\phi = \frac{1}{q}\left(q\theta - \chi - E_g\right) - \frac{k_B T}{q}\ln\left(y\right) + V_a, \; y = \frac{-N_{eff}}{2N_V} + \left[\left(\frac{N_{eff}}{2N_V}\right)^2 + \frac{N_C}{N_V}\exp\left(\frac{-E_g}{k_B T}\right)\right]^{1/2} \quad \backslash^* \text{ MERGEFORMAT (}$$

The BC for vacancies is homogenous Neumann for the entire simulation domain, i.e., $\boldsymbol{J}_V \bullet \hat{\eta} = 0$, indicating that the total number of vacancies in the domain is constant. This all-Neumann BC requires that all simulations involving the vacancy transport must be transient and run for sufficient time so as to reach steady-state, if steady-state results are needed, since DC-type simulations cannot produce unique solutions due to the all-Neumann BCs.

The BCs for the temperature equation are of three different types: (i) temperature is a user-defined constant at Dirichlet boundaries which mimic perfect heat sink, i.e., $T = T_{ext}$, where T_{ext} is a user-defined external temperature; (ii) inhomogeneous Neumann BC which mimics non-ideal heat sink, i.e., $\kappa_L \nabla T \bullet \hat{\eta} = \text{const}$ or $\kappa_L \nabla T \bullet \hat{\eta} = (T_{ext} - T)/R_{th} = G_{th}(T_{ext} - T)$, where κ_L is the thermal conductivity, R_{th} (G_{th}) is the thermal resistance (conductance) of a heat sink; (iii) homogenous Neumann BC at all other boundaries, i.e., $\kappa_L \nabla T \bullet \hat{\eta} = 0$.

2.4. Discretization and Stabilization

To implement the coupled equations, we first need to scale the equations into a form that is dimensionless. The reason for this scaling is that the basic unknown variables of electron density (n), hole density (p), and vacancy density (n_V) are usually large numbers (e.g., on the order of 10^{19} cm^{-3} for n) and can vary by many orders of magnitude in a device, which would lead to a highly ill-conditioned system matrix after discretization that is very difficult to solve. Hence, the standard practice is to introduce scaling factors and scale the equations into a dimensionless form. The most widely used scaling factors and the ones used in Charon are given in Table 1. Scaling Factors Used . After scaling, Eqs. * MERGEFORMAT (2)-* MERGEFORMAT (5) become

$$\lambda^2 \nabla \bullet \varepsilon_r \nabla(\phi - \theta) = -(p - n + n_V + C) \qquad \text{* MERGEFORMAT (24)}$$

$$\frac{\partial n}{\partial t} = \nabla \bullet \boldsymbol{J}_n - R_{net} \qquad \text{* MERGEFORMAT (25)}$$

$$\frac{\partial p}{\partial t} = -\nabla \bullet \boldsymbol{J}_p - R_{net} \qquad \text{* MERGEFORMAT (26)}$$

$$\frac{\partial n_V}{\partial t} = -\nabla \bullet \boldsymbol{J}_V \qquad \text{* MERGEFORMAT (27)}$$

$$\frac{\partial}{\partial t}\left(c_L T\right) - \nabla \bullet (\kappa_L \nabla T) = H \qquad \text{* MERGEFORMAT (28)}$$

Where all quantities are in scaled units.

Table 1. Scaling Factors for the Coupled Thermo-Electrical Transport Equations

Quantity	Symbol and Unit	Value
Coordinate scaling	X_0 [cm]	User-defined, 10^{-4} by default
Concentration scaling	C_0 [cm^{-3}]	User-defined, n_i by default
Diffusion coefficient scaling	D_0 [cm^2/s]	User-defined, D_n of Si by default
Temperature scaling	T_0 [K]	User-defined, 300 K by default
Voltage scaling	V_0 [V]	$k_B T_0 / q$
Mobility scaling	μ_0 [cm^2/(V.s)]	D_0 / V_0
Source scaling	R_0 [cm^{-3}. s^{-1}]	$D_0 C_0 / X_0^2$
Time scaling	t_0 [s]	X_0^2 / D_0

Electric field scaling	E_0 [V/cm]	V_0 / X_0
Current density scaling	J_0 [A/cm^2]	qD_0C_0 / X_0
Heat generation scaling	H_0 [W/cm^3]	$c_{L0}T_0 / t_0$
Heat capacity scaling	c_{L0} [J/(cm^3.K)]	User-defined
Thermal conductivity scaling	κ_{L0} [W/(K.cm)]	$H_0X_0^2 / T_0$
Laplacian scaling	λ^2 [1]	$V_0\varepsilon_0 / (qC_0X_0^2)$

Next, the equations need to be discretized in the space and time domains. Both finite volume and finite element (FE) methods have been considered for spatial discretization. In the following, the FE discretization method is described for the coupled equations. Within the FE method, the equations need to be converted into the FE integral weak form. The Galerkin FE weak forms of the equations are given below

$$\lambda^2\varepsilon_r\int\nabla(\phi-\theta)\nabla wd\Omega-\int(p-n+n_V+C)wd\Omega=0 \quad \backslash^* \text{ MERGEFORMAT (29)}$$

$$\int\frac{\partial n}{\partial t}wd\Omega+\int\mathbf{J}_n\bullet\nabla wd\Omega+\int R_{net}wd\Omega=0 \quad \backslash^* \text{ MERGEFORMAT (30)}$$

$$\int\frac{\partial p}{\partial t}wd\Omega-\int\mathbf{J}_p\bullet\nabla wd\Omega+\int R_{net}wd\Omega=0 \quad \backslash^* \text{ MERGEFORMAT (31)}$$

$$\int\frac{\partial n_V}{\partial t}wd\Omega-\int\mathbf{J}_V\bullet\nabla wd\Omega=0 \quad \backslash^* \text{ MERGEFORMAT (32)}$$

$$\int c_L\frac{\partial T}{\partial t}wd\Omega+\int\kappa_L\nabla T\bullet\nabla wd\Omega-\int Hwd\Omega=0 \quad \backslash^* \text{ MERGEFORMAT (33)}$$

where w is the FE nodal basis function. For the time domain discretization, the backward Euler approach (i.e., implicit Euler) is used, which is an unconditionally stable method. Therefore, the numerical stability of the discretized equations depends mainly on the spatial discretization. Equations * MERGEFORMAT (29) and * MERGEFORMAT (33) are generally stable with the FE discretization and do not need using any stabilization scheme. However, Eqs. * MERGEFORMAT (30)-* MERGEFORMAT (32) are convection-diffusion problems, which are well-known to require stabilization when discretized by the FE method.

Three popular FE stabilization schemes have been considered and implemented, including the Streamline Upwind Petrov Galerkin (SUPG) [45], the Symmetrized Exponentially Fitted Flux Galerkin (Sym-EFFG) [46], and the non-symmetrized EFFG [47] methods. For the SUPG

and Sym-EFFG schemes, an additional stabilization term is added to the Galerkin weak forms of the carrier continuity equations, i.e., Eqs. * MERGEFORMAT (30)-* MERGEFORMAT (32), in order to improve numerical stability. For the following stabilization description, the electron continuity equation is used as an example. The same stabilization methods are also applied to the hole and vacancy continuity equations.

The SUPG stabilization term for the electron continuity equation takes the form of

$$\int \tau_n (\boldsymbol{v}_{n,eff} \bullet \nabla n)(\boldsymbol{v}_{n,eff} \bullet \nabla w) d\Omega,$$

$$\text{where } \tau_n = \frac{1}{\sqrt{\boldsymbol{v}_{n,eff}^T \boldsymbol{g}_c \boldsymbol{v}_{n,eff}}} \left[\coth(p_n) - \frac{1}{p_n} \right],\ p_n = \frac{\sqrt{\boldsymbol{v}_{n,eff}^T \boldsymbol{g}_c \boldsymbol{v}_{n,eff}}}{D_n \left\| \boldsymbol{g}_c \right\|}. \qquad \text{* MERGEFORMAT (34)}$$

where $\boldsymbol{v}_{n,eff}$ is the electron effective velocity vector, $\boldsymbol{g}_c$ is the finite element contravariant tensor, D_n is the electron diffusion coefficient, and p_n is the electron Peclet number. The effective velocity in the stabilization term comes from the current expressions. After scaling, the currents in Eqs. * MERGEFORMAT (7)-* MERGEFORMAT (9) become

$$\boldsymbol{J}_n = n(-\mu_n \nabla \phi + \mu_n \nabla T) + D_n \nabla n = -n\boldsymbol{v}_{n,eff} + D_n \nabla n,\ \boldsymbol{v}_{n,eff} = \mu_n \nabla \phi - \mu_n \nabla T \quad \text{* MERGEFORMAT (35)}$$

$$\boldsymbol{J}_p = p(-\mu_p \nabla \phi - \mu_p \nabla T) - D_p \nabla p = p\boldsymbol{v}_{p,eff} - D_p \nabla p,\ \boldsymbol{v}_{p,eff} = -\mu_p \nabla \phi - \mu_p \nabla T \quad \text{* MERGEFORMAT (36)}$$

$$\boldsymbol{J}_V = n_V (\boldsymbol{v}_V - D_T S_V \nabla T) - D_V \nabla n_V = n_V \boldsymbol{v}_{V,eff} - D_V \nabla n_V,\ \boldsymbol{v}_{V,eff} = \boldsymbol{v}_V - D_T S_V \nabla T \quad \text{* MERGEFORMAT (37)}$$

It is seen that the effective velocity includes the drift component due to the electric field as well as the temperature gradient contribution. The τ parameter and the integrand of the SUPG stabilization term are evaluated at each integration point inside a finite element. There are a variety of choices described in the literature for the τ parameter. A certain choice of the τ parameter may work well for one set of problems, but may not be good for another set of problems, hence it is an art to choose the right τ expression to achieve the desired stabilization for a given problem.

The Sym-EFFG stabilization term is given below

$$\int \tilde{\Theta}(n) \bullet \tilde{\Theta}(w) d\Omega = \int \sum_{e_{ij} \in E(\Omega)} \theta_{ij} (n_j - n_i) \boldsymbol{u}_{ij} \bullet \sum_{e_{ij} \in E(\Omega)} \theta_{ij} (w_j - w_i) \boldsymbol{u}_{ij} d\Omega \quad \text{* MERGEFORMAT (38)}$$

with

$$\theta_{ij} = \sqrt{D_{ij} p_{ij} \left(\coth(p_{ij}) - \frac{1}{p_{ij}} \right)},\ p_{ij} = \frac{v_{ij} h_{ij}}{2 D_{ij}}$$

where $E(\Omega)$ denotes a finite element, e_{ij} denotes an edge starting with the node i and ending with the node j in an element, D_{ij} is the edge diffusion coefficient, v_{ij} is the effective edge velocity, h_{ij} is the edge length, p_{ij} is the edge Peclet number, and $\boldsymbol{u}_{ij}$ is the edge basis vectors. n_i and n_j are the electron density at node i and j, while w_i and w_j are the FE nodal basis function at node i and j. It is seen that the Sym-EFFG stabilization uses the edge lifting technique and results in symmetric diffusion for stabilization. Compared to the SUPG scheme, the Sym-EFFG stabilization does not use any tunable parameter. Furthermore, it contains the SUPG stabilization term with the choice of τ given in Eq. * MERGEFORMAT (34) and crosswind diffusion (e.g., in the direction perpendicular to the dominant velocity direction), as shown in Eq. * MERGEFORMAT (39)

$$\tilde{\Theta}(n)\bullet\tilde{\Theta}(w)\approx\tau_{\alpha}(\boldsymbol{v}_{eff}\bullet\nabla n)(\boldsymbol{v}_{eff}\bullet\nabla w)+\sum_{\mu\in\{v_{\perp1},v_{\perp2}\}}\sigma_{\alpha}\frac{\left\|\boldsymbol{v}_{eff}\right\|^2}{\left\|\mu\right\|^2}(\mu\bullet\nabla n)(\mu\bullet\nabla w)\quad\text{* MERGEFORMAT (39)}$$

where the first term on the right hand side represents the SUPG stabilization, and the second term indicates the crosswind diffusion. Therefore, the Sym-EFFG stabilization is more diffusive and consequently results in a better stabilization effect than SUPG when the crosswind velocity is strong. On the other hand, if the crosswind velocity is small, the Sym-EFFG and SUPG methods produce a similar stabilization effect.

The non-symmetrized EFFG method does not add a stabilization term to the Galerkin weak form, but directly modifies the weak form. Namely, instead of using the nodal current flux vector as in the Galerkin weak form, the EFFG method uses the edge-lifted current flux given by Eq. * MERGEFORMAT (41)

$$\int\frac{\partial n}{\partial t}wd\Omega+\int\boldsymbol{J}_{nE}\bullet\nabla wd\Omega+\int R_{net}wd\Omega=0\quad\text{* MERGEFORMAT (40)}$$

$$\boldsymbol{J}_{nE}=\sum_{e_{ij}\in E(\Omega)}J_{ij}\boldsymbol{u}_{ij}=\sum_{e_{ij}\in E(\Omega)}\frac{h_{ij}v_{ij}}{2}\left[n_j(\coth p_{ij}-1)-n_i(\coth p_{ij}+1)\right]\boldsymbol{u}_{ij},\ p_{ij}=\frac{v_{ij}h_{ij}}{2D_{ij}}\quad\text{* MERGEFORMAT (4}$$

The EFFG method is the foundation from which the Sym-EFFG scheme was derived. The two methods are the same for Cartesian mesh, but the Sym-EFFG method is more diffusive than EFFG for non-Cartesian mesh.

The three stabilization schemes were applied to the coupled thermo-electrical transient simulations of a titanium oxide memristor defined with a uniform Cartesian mesh. For this problem, the dominant velocity is along the direction of the device length, hence the crosswind velocity is negligible. Additionally, the mesh is uniform in Cartesian coordinates. The three

stabilization schemes are expected to produce nearly the same stabilization effect. Figure 2 shows the electron density color contour plots at the steady state obtained by applying the three stabilization schemes to the coupled thermo-electrical transient simulations of a titanium oxide memristor. It is evident that when no stabilization is used in solving the problem, the electron density shows clear spatial oscillations in the right-side region as shown in the top left panel, whereas the three stabilization schemes produce the same results, as expected.

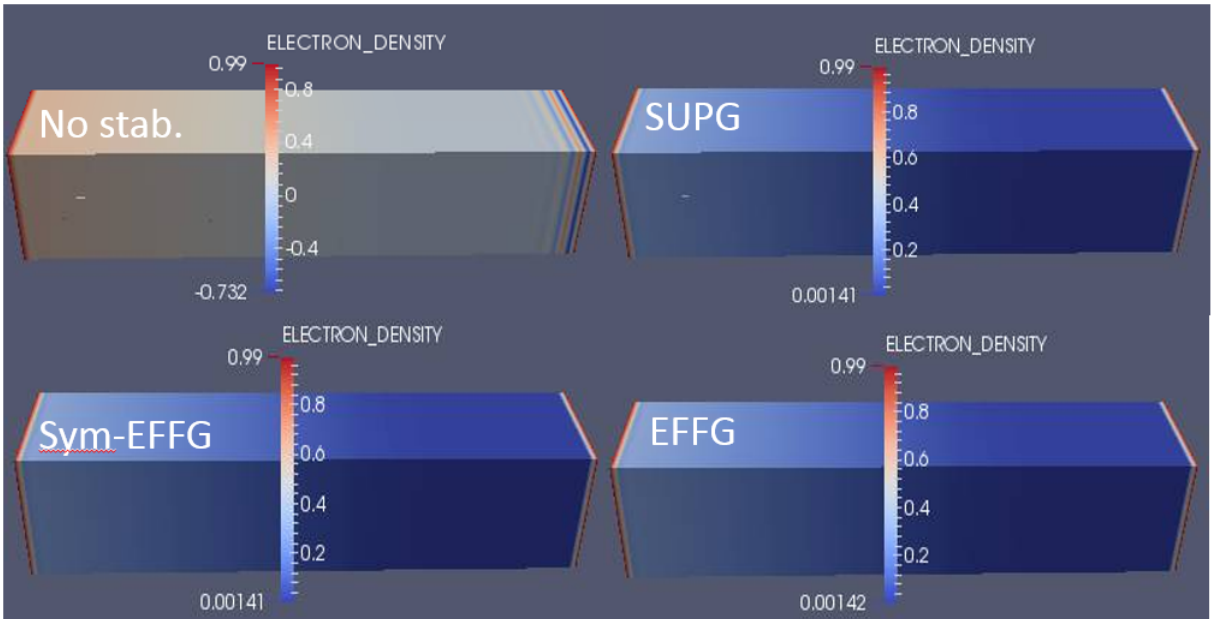

Figure 3. Electron density color contour plots at the steady-state obtained by applying the three stabilization schemes to the coupled thermo-electrical transient simulations of a titanium oxide brick

The fully-coupled transport equations with appropriate physical models and boundary conditions are implemented in Charon [48], a multi-dimensional parallel TCAD code developed at Sandia National Labs. Charon supports both finite element and finite volume discretization methods. For finite element discretization, it provides several stabilization schemes as described above. Charon is built on the open-source Trilinos libraries [49] that provide cutting-edge capabilities for solving nonlinear PDEs, including discretization utilities, nonlinear and linear solvers, MPI parallel capability, automatic differentiation, and many more. The device structure and mesh is created in Cubit [50] and then used as input to Charon. Simulation results from Charon can be visualized and analyzed in ParaView [51]. Charon can be used to simulate

arbitrary 1D/2D/3D device geometry, supports multi-physics capability (i.e., allowing for solving different equations in different regions), and allows for running thousands of large simulations simultaneously on high performance computing clusters.

3. VERFICATION OF THE TRANSPORT MODEL

In this chapter, the thermo-electrical transport model implemented in Charon is applied to simulate several scenarios corresponding to different levels of verification and validation of the Simulator.

3.1 Verification of the Heat Equation in a Silicon Block

As a first test, we apply the Simulator to solving the heat equation and compare the results to analytic solutions. That is, we use Charon to solve the dimensionless heat equation, i.e., Eq.* MERGEFORMAT (5), in a silicon block with different H and κ_L values, and compare the simulated results with analytic solutions. The simulated temperature color contours for different H and κ_L values are given in Figure 4 below, where the color legends indicate the temperatures in units of 300 K. The x-direction line cuts of Figure 4 results are plotted as symbols in Figure 5, where the black color corresponds to Figure 4(a), blue corresponds to Figure 4(b), and red corresponds to Figure 4(c). The analytic solutions of the heat equation are plotted as solid lines in Figure 5. It is clear that the simulated results very nicely coincide with the analytic solutions, which verifies the accuracy of the implemented heat model.

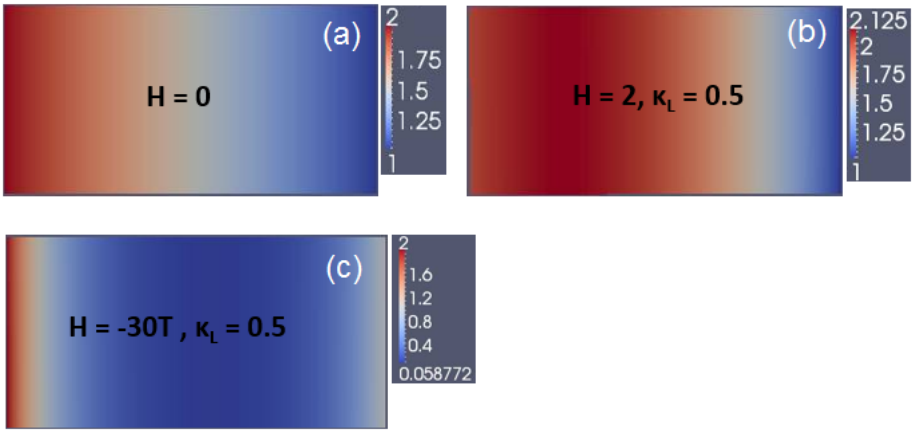

Figure 4. Simulated temperature color contours in a silicon block for different H and κ_L values.

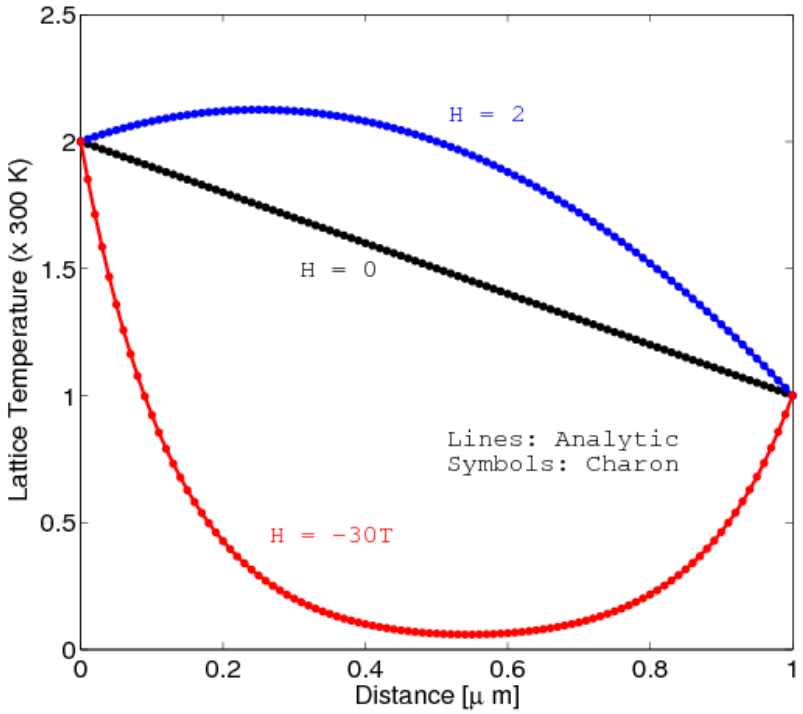

Figure 5. Comparison of simulated results with analytic solutions for the heat equation.

3.2 Verification of the Self-Heating in a Silicon PN Diode

This section verifies the electrical-thermal transport model for electrons and holes in a silicon PN diode. The Charon simulator is used to solve the Poisson equation, the electron and hole continuity equations, and the temperature heat equation, while the vacancy continuity equation is not solved here. This model allows us to simulate the self-heating effect in a semiconductor device, and is used to simulate a silicon PN diode under three different scenarios. For all three cases, the simulated silicon PN diode was arbitrarily chosen to be 1-μm long and 0.5-μm wide with the abrupt PN junction located at 0.5-μm.

The first two scenarios [i.e., case (A) and (B)] are shown in Figure 6, where the acceptor and donor doping are both equal to 10^{16} cm^{-3} (i.e., Na = Nd = 10^{16} cm^{-3}). The difference between the two cases is the temperature boundary condition: the temperature is fixed at 300 K at the two side boundaries for case (A), while the temperature is set to 600 K at the left side boundary and 300 K at the right for case (B). The carrier mobilities were computed using the Arora model [52]. The Shockley-Read-Hall (SRH) recombination model was enabled with concentration dependent carrier lifetimes [53]. Due to the relatively low doping, Boltzmann statistics was used. The thermal conductivity was computed using the temperature dependent model in Ref. [54], while

the heat capacity value was irrelevant here since the simulations were performed in the steady-state regime.

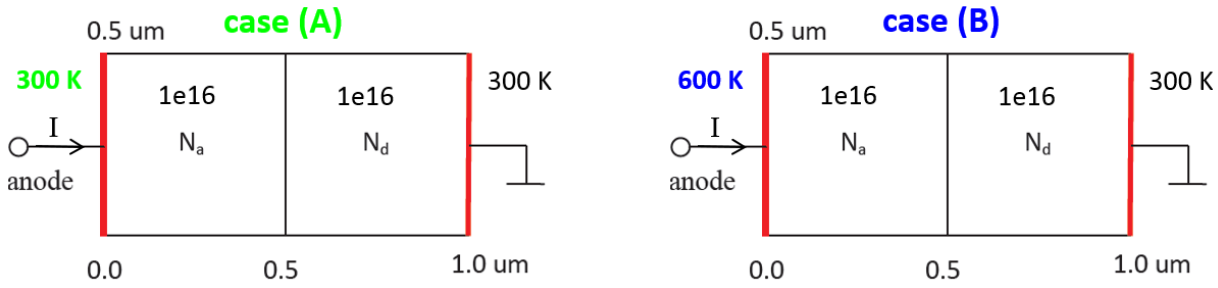

Figure 6. Test case (A) of the PN diode with Na = Nd = 1e16 cm^{-3} and T = 300 K at the two side boundaries; test case (B) with the right side fixed at 300 K while the left side set to 600 K.

The simulated current-voltage relations for cases (A) and (B) are plotted in Figure 7, together with the isothermal simulation results that were obtained by solving the Poisson equation simultaneously with the electron and hole continuity equations for a constant temperature of 300 K. It is seen that for the simulated voltage range, the currents of case (A) are nearly the same as those of the isothermal case, due to the fact that the Joule heating in case (A) was negligible and the side boundaries were fixed at 300 K. On the other hand, the results of case (B) are obviously different from case (A) and the isothermal case, especially for voltages less than 0.9 V. The large difference is because case (B) has a significant temperature gradient across the device, which contributes significantly to the current, especially for lower voltages. In fact, for voltages <= 0.3 V, the contribution from the temperature gradient is so dominant that the current is in an opposite direction as indicated by the empty squares.

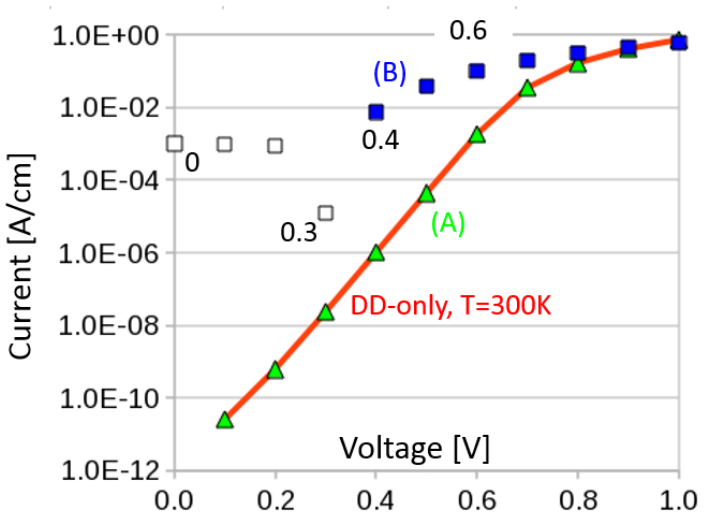

Figure 7. Current-voltage relations for the cases (A) and (B) given in Figure 6 and for the isothermal case.

The above two examples demonstrate that the coupled thermo-electrical transport model in Charon for electrons and holes indeed produces expected qualitative results for a silicon PN diode. It is noted that both cases produce very small Joule heating due to the relatively low doping and moderate voltage bias, and hence the self-heating effect is not visible. To observe the self-heating effect due to Joule heating and to perform quantitative comparison, a third example [case (C)] was created, which used the same silicon PN diode structure but with a high doping value of Nd = Na = 10^{19} cm^{-3}. The two side boundaries were also fixed at 300 K, similar to case (A). To quantitatively verify the accuracy of the thermo-electrical transport model, the Charon simulation results were compared with those results obtained using Atlas [55]. The simulated current-voltage curves are shown in Figure 8, and the spatial temperature profiles under several voltages are given in Figure 9.

It is clear from Figure 8 that the Charon simulation results (noted as Charon2 in the figure legend) agree very well with those of Atlas for both isothermal and non-isothermal cases. Due to the significant Joule heating at high bias (above 1.4 V), the simulated non-isothermal currents are substantially lower than the isothermal values, which is a well-known self-heating effect in semiconductor devices. The temperature profiles in Figure 9 show that the two codes produce similar temperatures for voltages £ 1.6 V. However, a peak difference on the order of 25% is observed at 1.8 V between the two codes. This relatively large difference in temperature at very high bias was not thoroughly investigated due to project time constraints, but fortunately, it

produces only about a 5% difference in currents between Charon and Atlas because the drift term dominates the current at such high bias.

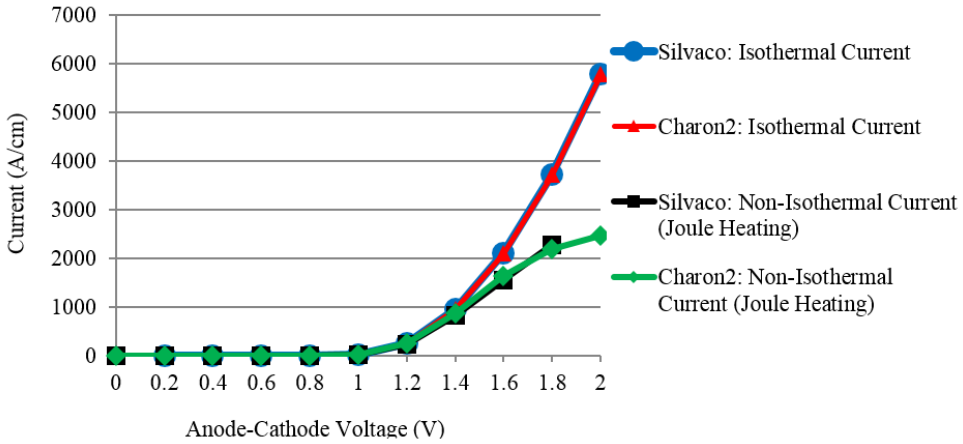

Figure 8. Comparison of current-voltage curves between Charon and Atlas for a silicon PN diode.

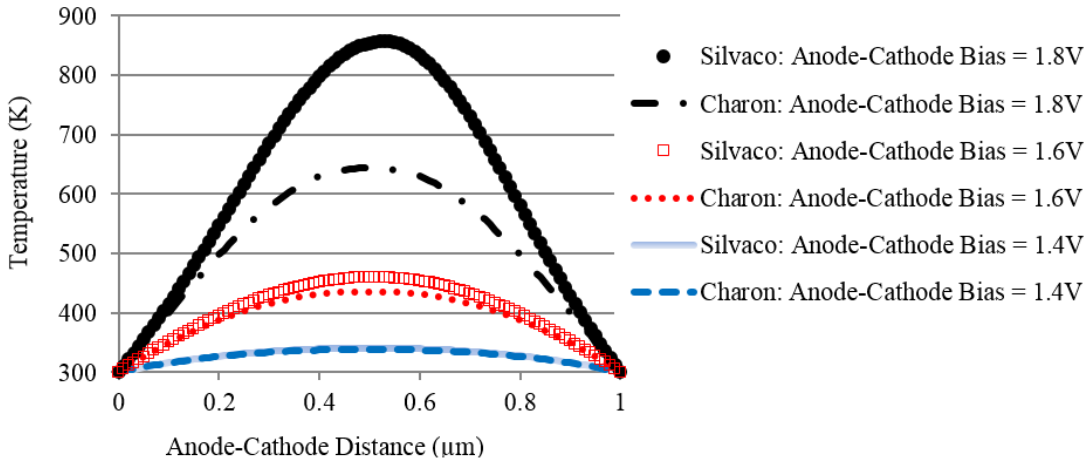

Figure 9. Comparison of temperature spatial profiles under several bias conditions between Charon and Atlas for the silicon PN diode.

3.3 Simulation of Titanium Oxide Memristor

This section verifies the isothermal drift-diffusion model for electrons, holes, and vacancies. The Charon simulator is used to simulate the carrier transport in a titanium oxide (TiOx) memristor, where the Poisson equation and the continuity equations for electrons, holes, and vacancies are solved, while the temperature is fixed at 300 K. The simulation is based on the TiOx memristor in Ref. [56], which is a 50-nm long TiOx film containing charged mobile n-type vacancy dopants with a distribution confined by the left and right electrodes and charged fixed p-type dopants. The left electrode is electrically grounded, while the right electrode is connected to a voltage source. For simulation and comparison purposes, the device is treated as 1D, though Charon can be equally applied to simulate 1D/2D/3D devices. Charon simulation results are compared with those of Ref. [56] for verification.

Figure 10 compares the simulated stationary resistance states between Charon and Ref. [56] for different positive voltages applied to the right-hand electrode. It is clear that all of the Charon results are in excellent agreement with those of the reference. The left column corresponds to the simulation results of Charon, while the right column represents to those of the reference. In panel (a), the black dotted, solid, dashed, and dot-dashed lines correspond to the equilibrium concentration profiles for the vacancy density, $N_D(x)$, under zero bias with N_D^* / N_{D0} ratios equal to 0.01, 0.1, 1, and 10, while the concentration of immobile acceptors is always $N_A/N_{D0} = 0.01$. The acceptors are uniformly distributed through the device. N_D^* is the average concentration of mobile vacancies, i.e., $N_D^* = \int N_D(x)dx / L$, with L being the length of the device. N_{D0} is set to 5×10^{20} cm^{-3}. In panels (a-c) the colored lines represent the steady-state profiles of the corresponding property for several applied voltages and $N_D^* / N_{D0} = 0.1$. The voltages in the reference are expressed in units of the thermal voltage, $V_0 = k_BT/q$, while the same set of voltages are expressed in units of Volts in the Charon results.

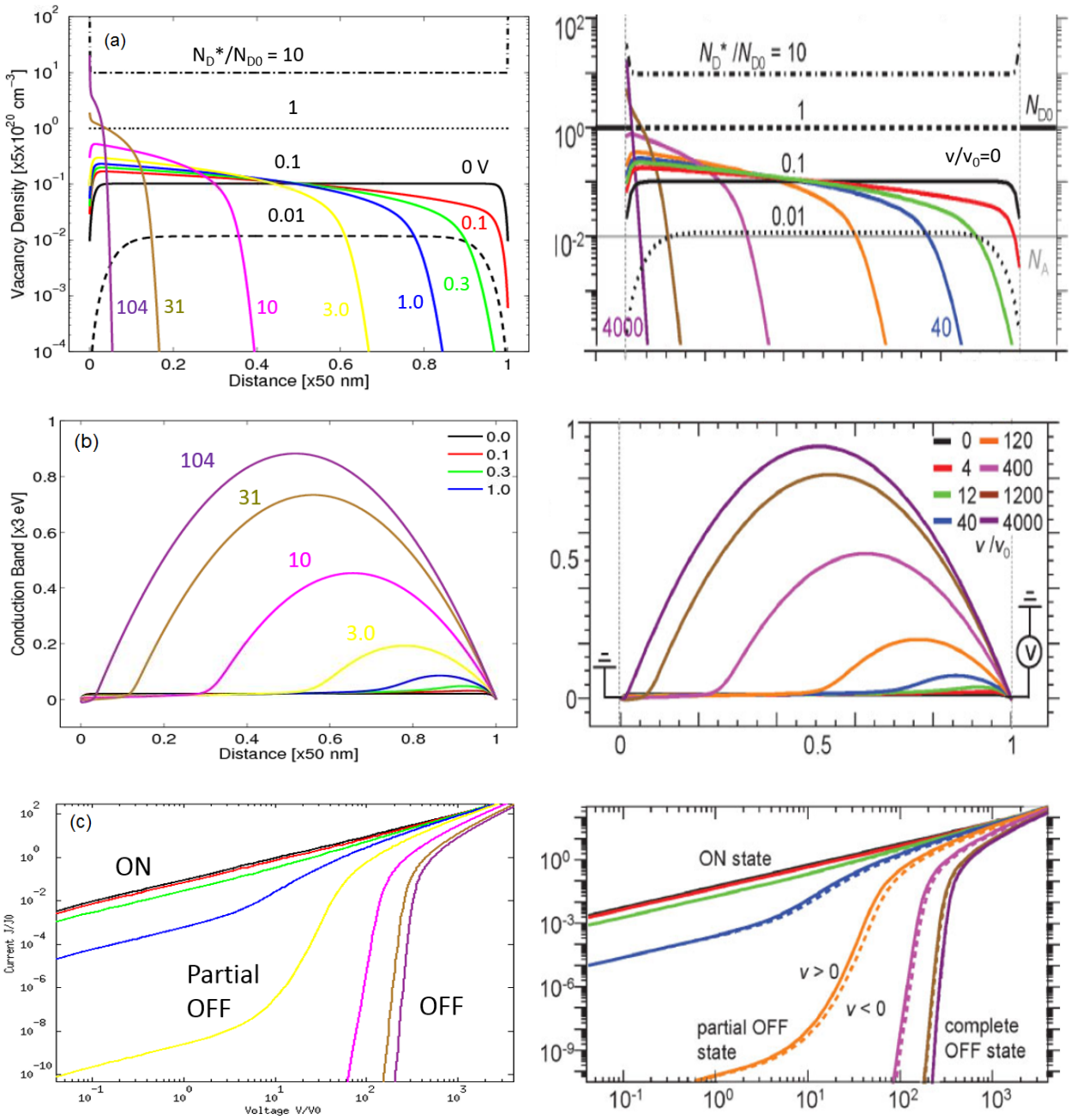

Figure 10. Comparison of stationary resistance states between Charon (left panel) and the reference (right panel) for different positive voltages applied to the right-hand electrode: (a) mobile vacancy concentration, (b) zero-bias potential, and (c) frozen configuration I-V characteristics for positive voltage sweeps.

Each curve in panel (a) was obtained by running a transient Charon simulation for a long enough time to reach steady state at a given voltage, and then the vacancy spatial profile was

extracted at steady state. As the applied voltage at the right electrode increases, the steady-state vacancy profiles are pushed further away from the right side. For each steady-state vacancy profile in panel (a), we froze the vacancy profile (i.e., the vacancies behave as immobile n-type dopants) and ran Charon drift-diffusion simulations without the vacancy continuity equation to obtain the DC current-voltage curves from which the resistances can be extracted. Panel (b) shows the conduction band profiles at zero bias for the frozen steady-state vacancy profiles. The band profiles indicate that a higher positive voltage at the right electrode causes positive mobile vacancies to drift further away from the right and results in effectively complete mobile vacancy depletion from the right side. Once the concentration of mobile vacancies in this region falls below that of the fixed acceptors, the device doping profile goes from n^+-n-n^+ to n^+-n-p-n^+. The p-type region produces a potential energy barrier for electrons, a barrier which becomes higher for a larger applied voltage than that was used to produce the frozen steady-state vacancy profiles. The corresponding current-voltage curves are shown in panel (c) for the frozen steady-state vacancy profiles in panel (a). It is seen that the device indeed shows an ON-state with the lowest resistance and also an OFF-state characterized by a strongly nonlinear I-V relation.

Figure 11 shows a comparison of dynamical vacancy spatial profiles between Charon (left panel) and the reference (right panel). It is evident that Charon results agree very well with those in the HP paper, except that the time scale may be different, due to the unknown t_0 parameter used in the paper. Panel (a) shows the changing of the vacancy profile with time as the device switches from ON-state to OFF-state due to a positive 3 V applied to the right electrode. Initially, the vacancies are nearly uniformly distributed in the device, which results in a low resistance state, defined as ON-state. As a positive voltage is applied to the right side, vacancies drift towards the left side due to their positive charges. As the time increases, more vacancies move to the left side, and a potential barrier is formed in the right region, turning off the device. If the positive voltage is applied for a long enough time, the drift of vacancies will be balanced by the vacancy diffusion, leading to a steady-state OFF-state. Starting from the OFF-state, a negative 3V at the right electrode attracts the vacancies back toward the right side, as shown in panel (b). However, this time evolution of the vacancy distribution for switching back to the ON-state is not the time-reversed image of the OFF-switching motion, which results in the hysteresis characteristics of the TiOx memristor.

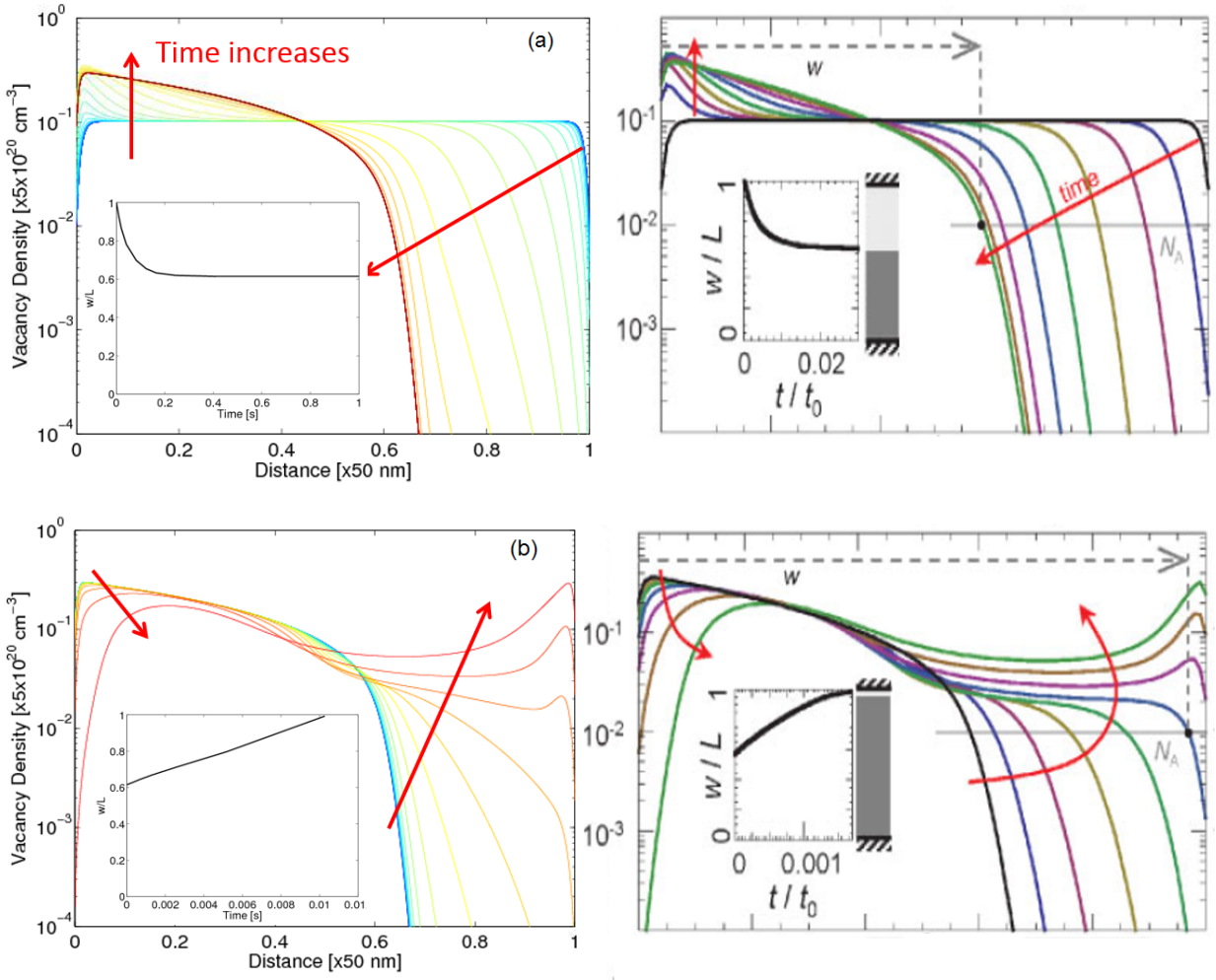

Figure 11. Comparison of dynamical vacancy profiles between Charon (left panel) and the reference (right panel): (a) ON-to-OFF switching with 3 V applied to the right electrode, and (b) OFF-to-ON switching with -3 V applied to the right electrode.

4. EFFECTS OF FIRST ORDER DEFECT CHEMISTRY ON THE DRIFT-DIFFUSION MODELING OF OXIDE-BASED MEMRISTORS

4.1 Introduction

As silicon-based memory technologies rapidly approach scaling limits, the semiconductor research community is actively pursuing novel, "Beyond Moore", device technologies to replace static random access memory (SRAM), dynamic RAM (DRAM), and flash memories. In fact, several candidate technologies have emerged in recent years as possible replacements for the aforementioned technologies [57,58]. One particularly promising technology that has been identified as such by the International Technology Roadmap for Semiconductors (ITRS) is resistive RAM, also known as redox, memristive memory, or ReRAM. Resistive memory is particularly attractive as a possible universal or storage class memory (SCM) technology due to its superb scalability, high switching speed, and low voltage operating characteristics [59,60,61,62, 63,64]. As schematically depicted in Figure 12, one possible realization of ReRAM is that of a metal-insulator-metal (M-I-M) "memristor" structure embedded within the metal layers of a silicon-on-insulator (SOI) technology [65].

Examples of commonly used insulators being investigated for ReRAM memory devices are transition metal oxides (TMOs) such as sub-stoichiometric tantalum pentoxide (TaO_x), titanium dioxide (TiO_x), and hafnium oxide (HfO_x) [61,62]. In this work we focus on tantalum oxide and titanium oxide memristors, as they are the subject of joint experimental efforts [66,67,68,69,70,71] .

The switching mechanism in TaO_x and TiO_x memristors that alters the state of the device between that of a high resistance off-state and that of a low resistance on-state is believed to involve defect chemistry reactions and migration of oxygen anions and neutral and positively charged oxygen vacancies. These processes lead to the formation of Ta- or Ti-rich conducting filaments [67,72]. Voltage sweeps conducted on these and other oxide-based memristors induce changes to the oxygen vacancy concentration profiles in the device. The result is a characteristic *I-V* hysteresis whereby one of the two paths of the hysteresis curve in the low-voltage bias regime represents a high resistance off-state and the other a low resistance on-state.

Shown in Figure 13 are the characteristic *I-V* hysteresis curves for an M-I-M experimental device that was fabricated and tested at Sandia National Laboratories (SNL). For the curves

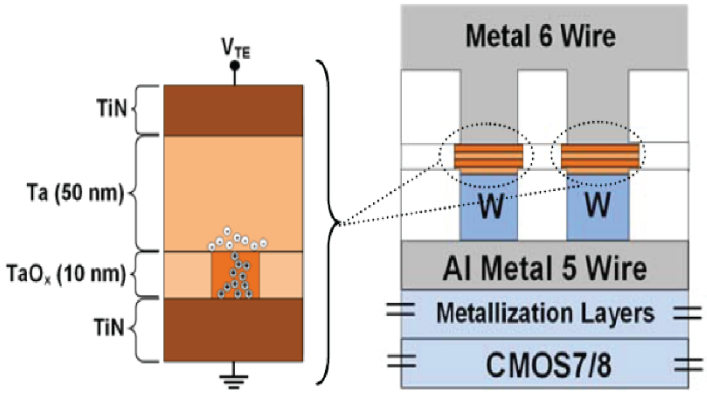

Figure 12. Schematic illustration of a plausible scheme to integrate a TaO_x memristor within the back-end metal layers of a SOI CMOS process [65].

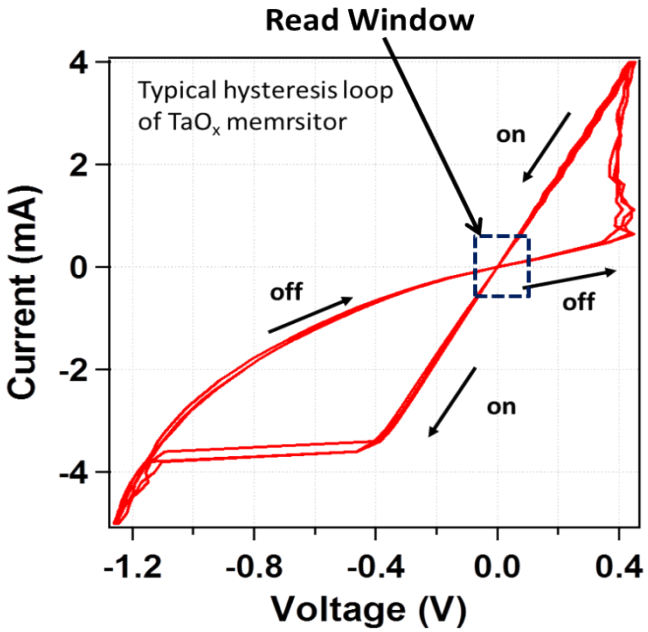

Figure 13. Hysteresis I-V characteristics of a TaOx memristor fabricated and tested at SNL. The arrows indicate the direction of the voltage sweep and the corresponding labels denote the state (high/low resistance) of the memristor. The dashed box indicates the read window.

shown in Figure 13, the memristor structure consisted of a 10nm thick TaO_x layer, a 15nm Ta layer, and top and bottom titanium nitride (TiN) electrodes that were 60nm and 20nm thick, respectively. The dashed box in Figure 13 denotes the memory-state "read" window. This is a low voltage regime that will not induce a change to the resistance of the device. Details of the fabrication process and experimental details are given in [73,74].

On/Off state changes to the device are caused by an alteration of the oxygen vacancy concentration profile in both the oxide (insulator) region and in any reactive electrodes. These changes are governed by the evolving oxide defect chemistry that is controlled by Joule heating and high electric-field processes. Accordingly, these devices require an initial electroforming cycle in order to induce oxygen-vacancy rich filament regions that form a low resistance channel. When applying higher voltages to the device, outside those of the read window, state changes can be induced.

A physics-based model for the device transport mechanisms, applicable for transport through the metal-insulator interfaces and in the bulk of the oxide, requires a treatment of tunneling at the metal-insulator interfaces. In this chapter, however, we present a phenomenological model of transport, relatively easy to implement in a computer code, in which we examine the impact of oxygen vacancy defect chemistry on transport in oxide-based memristors. This model is implemented as an extension to the well-established drift-diffusion formalism of semiconductor transport that has recently been applied to the simulation of memristor behavior by D.B. Strukov and R.S. Williams [75] (Note: We are also conducting a parallel research effort of a physics-based model [76], beyond the scope of this publication, which includes interface tunneling mechanisms).

In the Strukov and Williams model, memristor electrical characteristics are derived from a set of governing kinetic equations that describe the reactive transport of electrons, holes, and chemical species such as oxygen vacancies in the oxide portion of the memristor. However, the effects of reactive defect chemistry between oxygen vacancies are not included in their model. In this work, we include the effects of defect chemistry and despite not utilizing tunneling models to account for interface transport, we gain insight into the vacancy transport mechanisms, the strength of first order defect chemical reactions that occur in the oxide, and the resulting impact

of reactive defect chemistry on the device electrical characteristics. The details of our defect chemistry model are discussed in the next section.

4.2 REOS Model

Our defect chemistry model has been incorporated into the Sandia Radiation Effects in Oxides and Semiconductors (REOS) code [77]. For this phenomenological study, we model the system depicted in Figure 14, a simpler version than that of Figure 12, in which the 10nm length contacts are considered to act as Ohmic metal contacts for electron and hole current, in series with the oxide layer. The resistive properties of the contacts are therefore controlled by utilizing the doping concentration as a tuning parameter to calibrate the magnitude of the electronic current so as to be consistent with the effects of current limiting due to interface tunneling. Further details of Figure 14 will be explained in Section 4.3. Most importantly for our model, the metal contacts are assumed to be blocking for mobile oxygen vacancies (defects). Only electron and hole current flow is permitted across the oxide-metal interfaces.

REOS solves the reactive transport equations for a set of carrier species for rectangular device structures defined by a spatially non-uniform mesh. The governing kinetic equation is given as

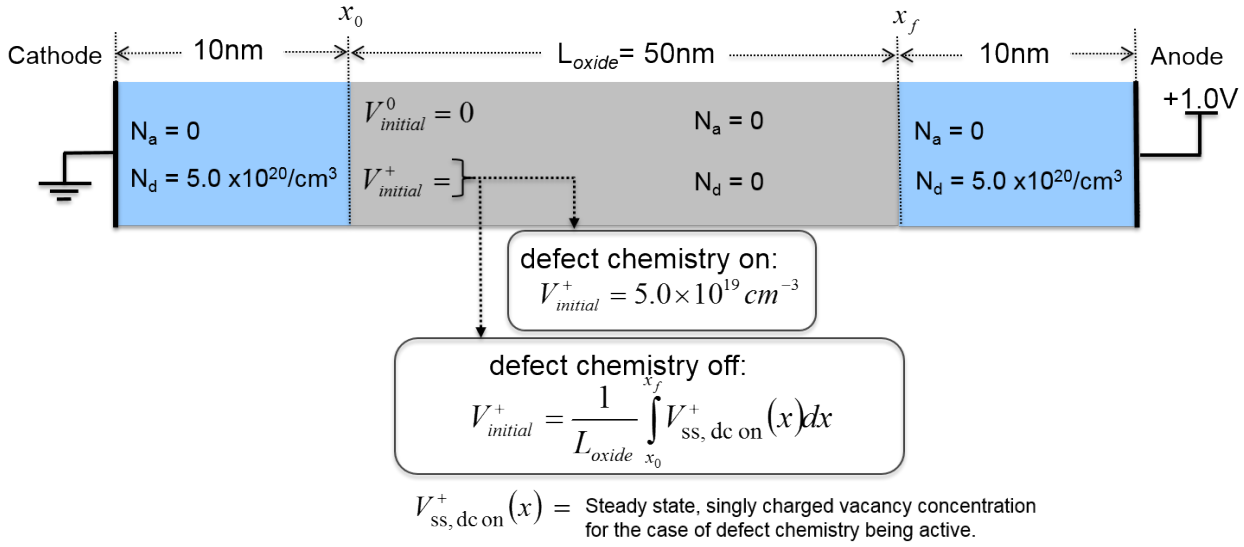

Figure 14. Schematic of simulated metal-insulating oxide-metal (M-I-M) memristor indicating the initial conditions for both types of simulations performed: Those with defect chemistry playing an active role in transport, and those without defect chemistry

being active. In both cases, the oxide/metal interfaces are assumed to be perfectly transmitting for electrons and holes (transport is negligible for holes) and perfectly blocking for mobile oxygen vacancies.

$$\frac{\partial c_i}{\partial t} = -\nabla \cdot \mathbf{J}_i + \sum_j \nu_{ij} R_j + G_i \qquad \text{* MERGEFORMAT (42)}$$

where $c_i \equiv c_i(\mathbf{r}, t)$ denotes the i^{th} species concentration as a function of position $\mathbf{r}$ and time t. $\mathbf{J}_i$ is the species current density, R_j is the reaction rate for defect reaction j, ν_{ij} is the stoichiometric coefficient that couples the strength of reaction j to the concentration of species i, and G_i is the net species generation rate for species generation processes other than those due to defect reactions, which we do not consider in this work, such as ionizing radiation incident upon the device. Furthermore, the species current density is given as

$$\mathbf{J}_i = -c_i \bar{\mu}_i \nabla \Phi_i \qquad \text{* MERGEFORMAT (43)}$$

where $\bar{\mu}_i$ is the species mobility, and Φ_i is the electrochemical potential. In Equation * MERGEFORMAT (43) the electrochemical potential is given as the sum of the electrostatic and chemical potential:

$$\Phi_i = -\phi + \mu_i \qquad \text{* MERGEFORMAT (44)}$$

where μ_i is the chemical potential for the i^{th} species.

The electrochemical potential of Equation * MERGEFORMAT (44), a central quantity in our calculations, is individually determined for all species. It governs the rate of all chemical reactions and all transport phenomena via the potential gradient of Equation * MERGEFORMAT (43). In thermal equilibrium, the electrochemical potential is constant throughout the device. An applied bias is manifested as the difference in the electrochemical potentials in the left and right-hand side electrodes, and the local densities of each carrier species are obtained from the energy difference between the species band edge and the electrochemical potential [78]

For the case of electrons in the near equilibrium approximation, we denote the chemical potential in Equation * MERGEFORMAT (44) as follows [79]:

$$\mu_n = \mu_{0,n} + kT \log\left(n / N_c\right) \qquad \text{* MERGEFORMAT (45)}$$

where $\mu_{0,n}$ is a material dependent constant, n is the electron density, and N_c is the conduction band thermal density of states. Additionally, the electrostatic potential ϕ in Equation * MERGEFORMAT (44) is obtained by self-consistently solving the Poisson equation with Equations * MERGEFORMAT (42) and * MERGEFORMAT (43) and is given as

$$\nabla^2 \phi = -\rho/\varepsilon \qquad \text{* MERGEFORMAT (46)}$$

where ε is the relative permittivity of the oxide, and the total charge density is given as $\rho = \sum_i z_i c_i$ in which z_i is the charge of species concentration c_i.

In the drift-diffusion approximation that REOS uses to solve the Boltzmann Transport Equation (BTE), the key contribution to the current density arises from electrons and Equation * MERGEFORMAT (43) can thus be expressed as

$$\mathbf{J}_n = q n \bar{\mu}_n \nabla \phi + D_n \nabla n \qquad \text{* MERGEFORMAT (47)}$$

where n is the electron density, ϕ is the electrostatic potential, $\bar{\mu}_n$ is the electron mobility, and D_n is the electron diffusion coefficient. For all carrier species in our model the diffusion coefficient and mobility are related by the Einstein relationship,

$$\bar{u}_i = D_i/kT \qquad \text{* MERGEFORMAT (48)}$$

Furthermore, REOS calculates displacement current in the determination of transient quantities, and Joule heating is accounted for by solving the Fourier heat equation self-consistently with Equation * MERGEFORMAT (42). For the results presented in this chapter, however, we assume a constant lattice temperature of T=300K for all species.

As regards to the inclusion of defect chemistry in REOS, the electron emission-capture reaction in oxide-based memristors that occurs between neutral and single, positively charged oxygen vacancies [80] is the dominant defect chemistry mechanism of our model. We assume that the defect states form a set of dominant bands that exist on the order of ~0.1eV to ~0.3eV below the conduction band. Additionally, these shallow defect bands are likely to broaden within a few nanometers of the metal-oxide interfaces due to the presence of interface surface defect states. These assumptions support our assertion, beyond the scope of this paper, that a memristor

is similar to a leaky oxide-based capacitor in that the current transport through the device is governed by a common set of transport mechanisms [78].

Furthermore, although REOS can account for reactions involving double, positively charged oxygen vacancies, we omit such reactions as the defect level of double-charged vacancies is expected to be greater than 1.0eV below the conduction band [81]. Hence, the dominant electron emission-capture defect reaction that we consider in our model is given as

$$V^+ + e \leftrightarrow V^0 \qquad \text{* MERGEFORMAT (49)}$$

where V^0 and V^+ indicate a neutral and a positively charged defect state, respectively, and e indicates the negatively charged electron that is captured or emitted from the bound defect state. The net generation rate of electrons into the conduction band for this reaction, which is implemented in our model via the second term on the right side of Equation * MERGEFORMAT (42) is given as

$$n_{n1}R_1 = k_{1f}\left[V^+\right]n - k_{1r}N_{th}\left[V^0\right] \qquad \text{* MERGEFORMAT (50)}$$

In Equation * MERGEFORMAT (50), n is the electron density, and N_{th} is the thermal density of states. The forward and reverse reaction rates, k_{1f} and k_{1r} respectively, are defined as

$$k_{1f} = \sigma v_{th} e^{-E_f/kT} \qquad \text{* MERGEFORMAT (51)}$$

$$k_{1r} = \sigma v_{th} e^{-E_r/kT} \qquad \text{* MERGEFORMAT (52)}$$

where σ is the capture cross-section, and v_{th} is the thermal velocity. E_f and E_r are the activation energy levels for forward and reverse reactions, respectively. These activation energies define the energy level of the defect state relative to that of the conduction band. In these calculations we set E_f equal to zero as the forward reaction is considered to have no thermal dependence and is governed only by the Coulomb force. As previously mentioned, the choice for the range of defect level energies of E_r ~ -0.1eV to -0.3eV is consistent with our assertion, to be discussed in a future publication [78] that the mechanisms of memristor transport are similar to those of leakage currents in oxide-based capacitors. Additionally, we define the capture cross section σ to be ~1.0×10^{-12} cm^2 to ~1.0×10^{-14} cm^2 and the thermal velocity is proportional to the lattice temperature. Other quantities in Equation * MERGEFORMAT (50) are previously defined. For calculations involving Joule heating, we use Dirichlet boundary conditions at the electrodes, and

typically set the lattice temperature at the contacts to be T=300K. Finally, while the study of Strukov and Williams [77] assumed a system with three non-reacting carrier species: electrons, holes, and mobile, positively, single-charged oxygen vacancies, in our model the transport of neutral vacancies via diffusion is accounted for by Equation * MERGEFORMAT (43) and the associated reactive defect chemistry noted by Equations * MERGEFORMAT (49)-* MERGEFORMAT (52).

Furthermore, in our model only electrons can penetrate the metal/oxide interfaces which are considered to be Ohmic. The oxygen vacancies are confined to the oxide layer. As the contacts are assumed to be blocking for vacancies, the total vacancy flux through the device is zero at all times, i.e.,

$$F_{V_p} + F_{V_0} = 0 \qquad \text{* MERGEFORMAT (53)}$$

where V_p and V_0 indicate the single-charged and neutral vacancy concentrations, respectively. The significance of Equation * MERGEFORMAT (53) is central to the analysis of our results and will be discussed further in the results section.

4.3 Simulation Procedure

In order to understand the impact of defect chemistry on the electrical characteristics of the prototypical memristor depicted in Figure 14, we conduct two sets of numerical experiments as follows. In the first set of calculations, we allow defect chemistry to play an active role in the transport. In these cases, the reaction of Equation * MERGEFORMAT (49) continuously alters the proportional contributions of neutral and single-charged vacancies to the current density until steady-state is achieved. An initial uniform concentration of oxygen vacancies in the oxide layer is present at the start of the simulation, a zero-bias condition. Then, a 1.0V bias is applied at the anode and all species (electrons, neutral and charged oxygen vacancies, and holes which are of negligible density) are allowed to undergo drift-diffusion movement and reach a steady-state condition. The steady-state physical quantities of interest, such as electron current and vacancy species concentration profiles for a given set of diffusion coefficients and defect energy levels, are then plotted and tabulated.

Next, we repeat the calculations for the condition of defect chemistry not playing any active role in carrier transport. In such cases, in order to maintain appropriate conservation of charge in

the device and make a fair comparison with the results for the case of defect chemistry being active, all simulation conditions remain the same as in the case of defect chemistry being active, except that the initial uniform concentration of mobile oxygen vacancies is now given as the steady-state average (i.e., integrated over the real-space volume of the oxide) concentration of single, positively charged oxygen vacancies for the case of defect chemistry being enabled. As mentioned, this methodology is graphically illustrated in Figure 14 in Section 4.2.

4.3 Simulation Results

For all results presented in this chapter, we use the M-I-M structure shown in Figure 14, where the simulated active oxide region has a thickness of 50.0nm and a constant cross-sectional area. Although we recognize that the oxide thicknesses of such prototypical memristors may be much smaller in actuality, on the order of 10.0nm or less, this particular structural implementation was chosen to be consistent that of [77]. Furthermore, we expect the results to be qualitatively extended to structures of lower dimensionality in which the resistivity of the oxide is postulated to be modulated by a moving "vacancy front" that results in a build-up of a tantalum (or titanium) rich conductive region extending from the oxide/metal interface at the cathode to the edge of the charged vacancy front within the oxide. Such a region acts as a conductive filament.

Following the simulation procedure discussed in Section 4.2 and represented in Figure 14, tabulated values of electron current are shown in Table 2 for various combinations of transport parameters for both types of simulations: Defect chemistry being active or turned off. In Table 2, results are not presented for cases in which $D_0 > D_p$ as such cases are considered to be unphysical.

In order to understand the values of electron current presented in Table 2, one must consider the total flux density F of single-charged and neutral vacancies. As previously mentioned, the contacts are assumed to be blocking for vacancies, and the total vacancy flux through the device is zero at all times. Hence, making use of Equation * MERGEFORMAT (48), if we expand the terms of Equation * MERGEFORMAT (53) for the vacancy flux, as was done for the case of electrons in obtaining Equation * MERGEFORMAT (47), we obtain

$$V_p \bar{m}_p \vec{E} - D_p \tilde{N} V_p - D_0 \tilde{N} V_0 = 0 \qquad \text{* MERGEFORMAT (54)}$$

In the formalism of the Boltzmann transport theory, it is well known that usage of the Einstein relationship is invalid for describing transport if the energy distribution of the carriers is beyond the near-equilibrium regime (i.e., carrier energies being on the order of only a few times that of the thermal energy). However, a more appropriate theory of Boltzmann transport through amorphous or polycrystalline oxides such as sub-stoichiometric Ta_2O_5 is currently lacking. Thus, we use Equation * MERGEFORMAT (54) as a starting point for our analysis. If the diffusion coefficients for both single-charged and neutral vacancies are considered to be equal, $D_p = D_0 = D$, then Equation * MERGEFORMAT (54) can be re-arranged as

Table 2. Electron current values with and without defect chemistry being active.
V_0 → neutral vacancy species, V_p → single-charged vacancy species.
E_r is defect band level relative to conduction band edge, bias voltage = 1.0V for all cases.

V_0 Diffusion Coef. (cm^2/sec) / V_p Diffusion Coef. (cm^2/sec)

V_p \ V_0	10^{-10}	10^{-9}	10^{-8}	10^{-7}	10^{-6}
10^{-10}	11.51 7.95				
10^{-9}	8.055 7.656	11.51 7.95			
10^{-8}	7.639 7.599	8.055 7.656	11.51 7.95		
10^{-7}	7.596 7.592	7.639 7.599	8.055 7.656	11.51 7.95	
10^{-6}	7.592 7.591	7.596 7.592	7.639 7.599	8.055 7.656	11.51 7.95

E_r = 0.0eV

V_0 Diffusion Coef. (cm^2/sec) / V_p Diffusion Coef. (cm^2/sec)

V_p \ V_0	10^{-10}	10^{-9}	10^{-8}	10^{-7}	10^{-6}
10^{-10}	6.752 2.792				
10^{-9}	3.169 2.450	6.752 2.792			
10^{-8}	2.396 2.312	3.169 2.450	6.752 2.792		
10^{-7}	2.297 2.288	2.396 2.312	3.169 2.450	6.752 2.792	
10^{-6}	2.286 2.285	2.297 2.288	2.396 2.312	3.169 2.450	6.752 2.792

E_r = -0.1eV

V_0 Diffusion Coef. (cm^2/sec) / V_p Diffusion Coef. (cm^2/sec)

V_p \ V_0	10^{-10}	10^{-9}	10^{-8}	10^{-7}	10^{-6}
10^{-10}	1.694 1.201				
10^{-9}	1.510 1.120	1.694 1.201			
10^{-8}	1.107 1.013	1.510 1.120	1.694 1.201		
10^{-7}	0.9819 0.9701	1.107 1.013	1.510 1.120	1.694 1.201	
10^{-6}	0.9628 0.9616	0.9819 0.9701	1.107 1.013	1.510 1.120	1.694 1.201

E_r = -0.2eV

V_0 Diffusion Coef. (cm^2/sec) / V_p Diffusion Coef. (cm^2/sec)

V_p \ V_0	10^{-10}	10^{-9}	10^{-8}	10^{-7}	10^{-6}
10^{-10}	0.8330 0.8205				
10^{-9}	0.8331 0.8202	0.8330 0.8205			
10^{-8}	0.8315 0.8166	0.8331 0.8202	0.8330 0.8205		
10^{-7}	0.8155 0.8000	0.8315 0.8166	0.8331 0.8202	0.8330 0.8205	
10^{-6}	0.8059 0.8048	0.8155 0.8000	0.8315 0.8166	0.8331 0.8202	0.8330 0.8205

E_r = -0.3eV

Upper box values = Electron current (x 1.0x10^{-8} A) - defect chemistry on
Lower box values = Electron current (x 1.0x10^{-8} A) - defect chemistry off

$$D\left(\frac{qV_p}{kT}\vec{E} - \nabla\left(V_p + V_0\right)\right) = 0 \qquad \text{* MERGEFORMAT (55)}$$

Inspection of Equation * MERGEFORMAT (55) reveals that the physical quantities in the brackets are independent of the value of the diffusion coefficient. Hence, the main diagonal terms in Table 2 are all identical for a particular defect energy level and mode of analysis (defect chemistry off or on), regardless of the actual value of the diffusion coefficient. As expected, when comparing the main diagonals of Table 2 for all four values of E_r (0.0, -0.1,- 0.2, and -0.3eV), one observes that the overall current decreases if the defect level becomes deeper relative to the conduction band edge, as fewer carriers are made available to contribute to transport. Furthermore, the current density is always higher for the case of defect chemistry being on, rather than being off. The reason for this can be understood by inspection of Figure 15, where we plot the steady-state concentration profiles of electrons, single-charged vacancies, and neutral vacancies for one representative case of Table 2, $E_r = 0.0\ \text{eV}$, $D_p = D_0 = 10^{-8}\ \text{cm}^2/\text{sec}$.

As observed in Figure 15, Equation * MERGEFORMAT (54) reveals that when defect chemistry is enabled, the neutral vacancy concentration in steady state does not evolve to a uniform spatial distribution as would happen if defect chemistry were not enabled. Rather, the gradient of the neutral vacancy concentration profile is given by the third term of Equation * MERGEFORMAT (54), $\tilde{N} V_0$. This neutral vacancy gradient allows a steady-state diffusion of neutral vacancies toward the anode of the device that does not occur without defect chemistry being enabled. Without defect chemistry enabled, the distribution of neutral vacancies would be uniform throughout the oxide region, as mentioned,

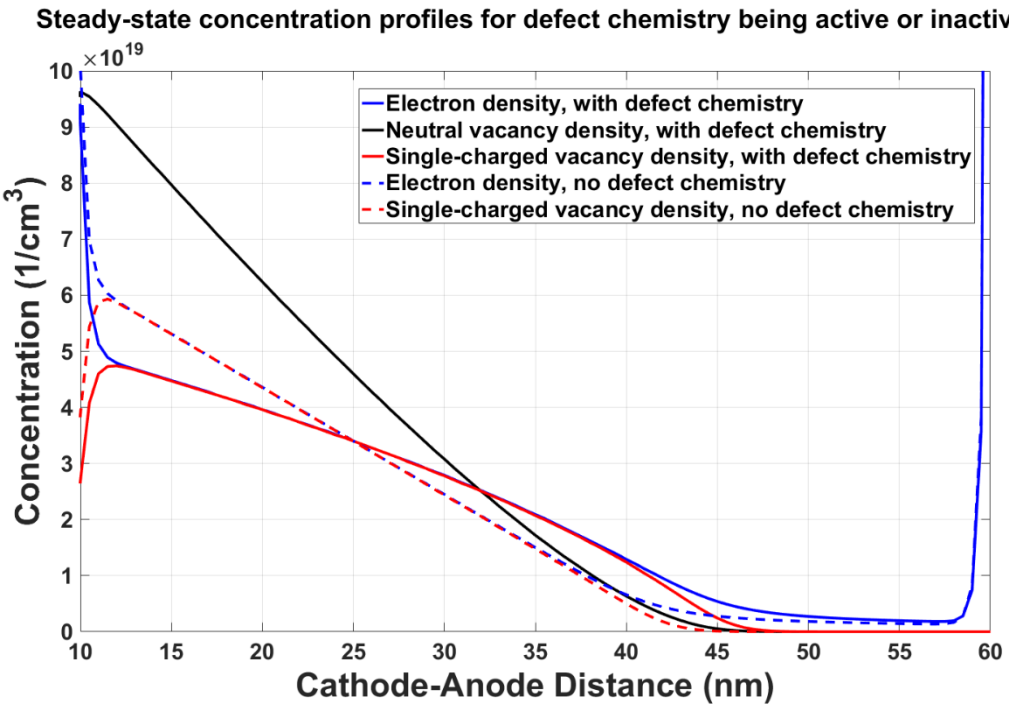

Figure 15. Steady-state species concentrations with and without defect chemistry being active. For this case the bias voltage equals 1.0V, and the neutral and single-charged vacancy diffusion coefficients are equal, $D_p = D_0$. The reverse and forward activation energies are zero. The results are qualitatively similar for other biases, unequal neutral and single-charged diffusion coefficients, or non-zero reverse activation energies.

and the net diffusion of neutral vacancies would be zero. Hence, in the situation with defect chemistry active, the strong diffusion of neutral vacancies toward the anode allows for a corresponding increase in the creation of single-charged vacancies and electron emission in the oxide near the anode, as compared to the case of no defect chemistry, via the reaction presented in Equation * MERGEFORMAT (49). The oxide therefore becomes more conductive nearer the side of the anode with the defect chemistry on, which consequently results in a corresponding increase in current as compared to the case of no defect chemistry being active. Hence, for defect chemistry being enabled, one can consider the effect of reactive defect chemistry in the oxide near the anode of the device as analogous to increasing the conductivity of a semiconductor by increasing the doping.

In order to understand the off-diagonal terms of Table 2, i.e., the cases of $D_p \neq D_0$, Equation * MERGEFORMAT (54) can similarly be re-arranged as follows,

$$\frac{D_p}{D_0} = \frac{\tilde{N} V_0}{\left(\tilde{N} V_p \exp\left(\frac{V_p}{kT} E\right) - \tilde{N} V_p\right)} \qquad \text{* MERGEFORMAT (56)}$$

In Equation * MERGEFORMAT (56), one observes that only the ratio of D_p to D_0, not the actual values of D_p and D_0, is relevant in obtaining the steady-state quantities of the right hand side (RHS) of Equation * MERGEFORMAT (56). Hence, in Table 2 the values of the electron current for the off-diagonal terms are equal along each diagonal for each of the two modes (defect chemistry off or on). Further analysis of the relationship of the relative magnitudes of the electron currents for both modes for the off-diagonal cases then follows the same reasoning as for the diagonal cases.

Additional insight into the characteristics of the transport mechanisms within the oxide can be gained by examining the drift and diffusion components of the steady-state species current densities for device operation with and without defect chemistry being active. Accordingly, in Figure 16 and Figure 17 we plot the steady-state drift and diffusion components of the vacancy and electron current densities, respectively, for the case of no defect chemistry being active. These plots correspond to the data and conditions of the results presented in Figure 15 ($E_r = 0.0\ \text{eV}, D_p = D_0 = 10^{-8}\ \text{cm}^2/\text{sec}$).

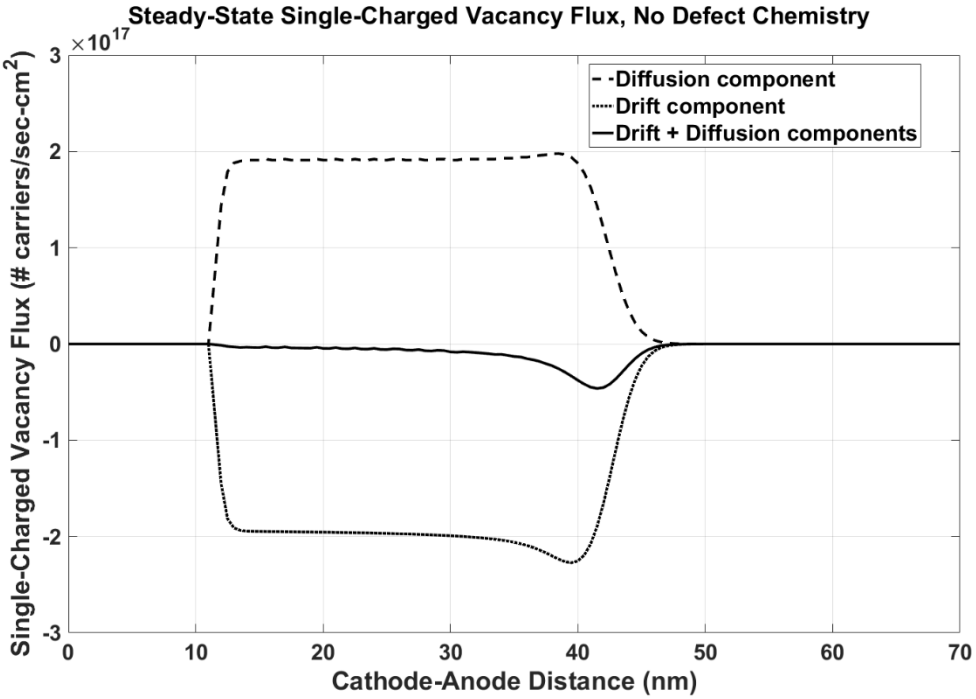

Figure 16. Components of single-charged vacancy flux for the case of no defect chemistry being active, corresponding to the curves shown in Figure 15.

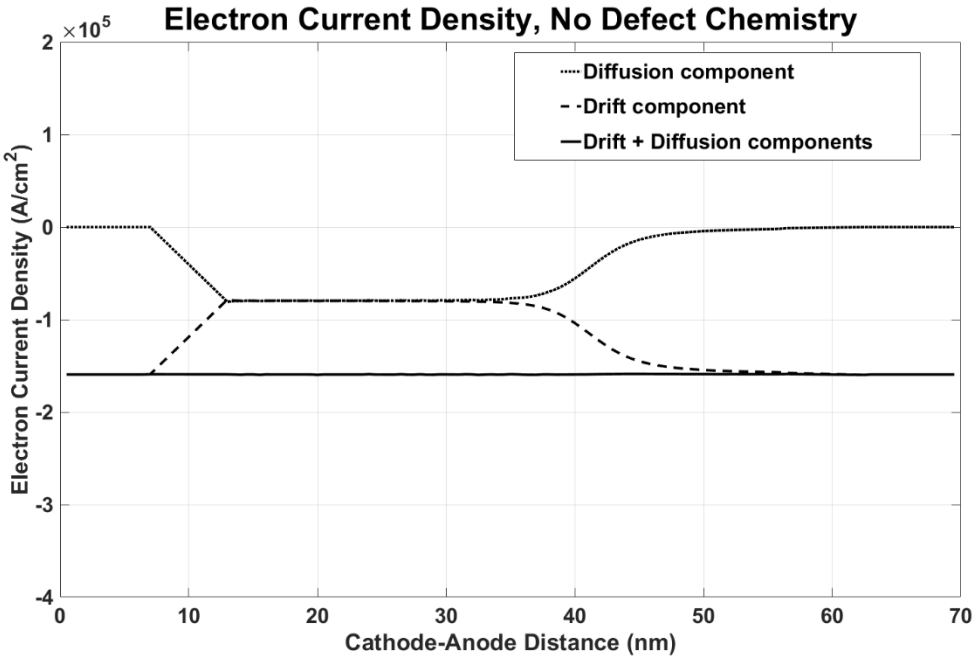

Figure 17. Components of electron current density for the case of no defect chemistry being active, corresponding to the curves shown in of Figure 15. The abrupt discontinuities at the left of the plot are due to numerical artifacts and are not physical.

As shown in Figure 16, the magnitudes of the drift and diffusion components of the single charged vacancy flux are equal and flow in opposite directions. This can be understood by noting that our convention is to define the direction of current to be positive for positive charge flowing from the left to the right in Figure 14. The results of Figure 16 and Figure 17 are therefore consistent with what would be expected upon inspection of the vacancy species flux equations, Equations * MERGEFORMAT (53) and * MERGEFORMAT (54). Because defect chemistry is inactive in this case, $\tilde{N} V_0 = 0$ in Equation * MERGEFORMAT (54), the drift and diffusion components of the single-charged vacancy flux have equal magnitude and are oppositely directed. Therefore, per our stated convention for defining the direction of current density (and noting that electric current is obtained by multiplying the species flux by the coulomb charge) the single-charged vacancy drift current thus flows from the anode to the cathode and the diffusion current flows from the cathode to the anode (i.e., the direction of flux is opposite to the single-charged vacancy concentration gradient presented in Figure 15), consistent with Equation * MERGEFORMAT (54) and the data of Figure 15. Furthermore, because charge neutrality must be maintained in the device, we note that in Equation * MERGEFORMAT (54), on average, $\frac{\partial V_0}{\partial x} = \frac{\partial n}{\partial x}$, and thus Equation * MERGEFORMAT (54) also necessitates that the magnitudes of the electron drift and diffusion currents must also, on average, be equal as indicated in Figure 17. However, because the charge is of opposite sign for the electrons as compared to the single-charged vacancies, the drift and diffusion components of the electron current density flow in the same direction resulting in a net electron current which is finite, and the zero-flux boundary condition of Equation * MERGEFORMAT (53) does not hold.

For the cases of defect chemistry being active, the situation is as depicted in Figure 18 for the vacancy flux and in Figure 19 for the electron current. As observed in Figure 18, the magnitudes of the drift and diffusion components of the single-charged vacancy flux are not equal, although they are still oppositely directed as expected. Similarly, as observed in Figure 19, the magnitude of the diffusion and drift components of the electron current are not equal, unlike for the case with no defect chemistry. In this case, the magnitude of the electron drift current is greater than that of the diffusion component.

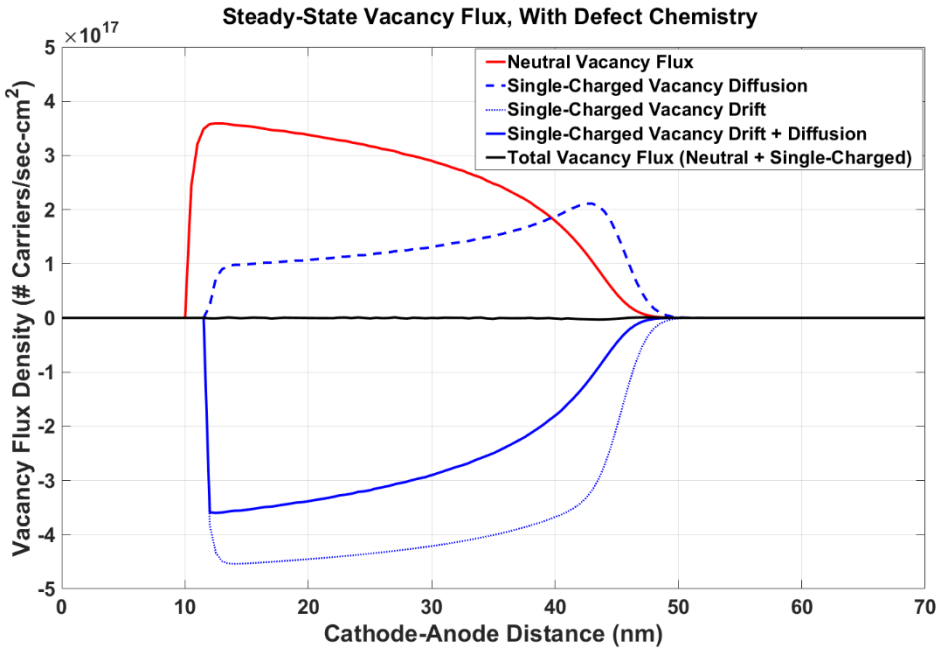

Figure 18. Components of vacancy flux for both species, neutral and single-charged, for the case defect chemistry being active, corresponding to the curves shown in Figure 15.

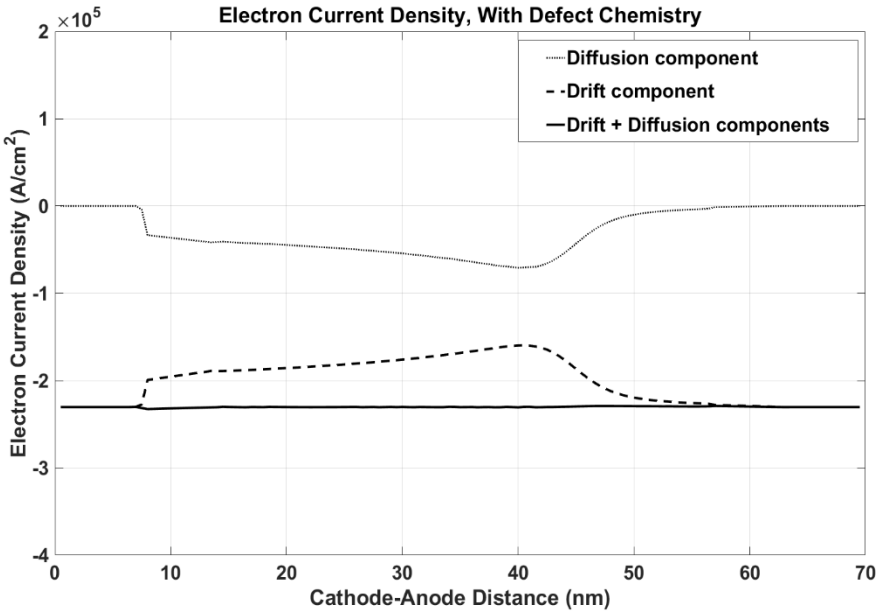

Figure 19. Components of electron current density for the case of defect chemistry being active, corresponding to the curves show in Figure 15.

The situation with defect chemistry being active is made clear by inspection of Equation * MERGEFORMAT (54) and noting that the summation of the total number vacancies in the oxide, neutral and single charged, must remain constant at all times. Keeping this in mind, one can re-arrange and integrate Equation * MERGEFORMAT (55) over the length of the oxide region, again making use of Equation * MERGEFORMAT (48), as follows

$$\frac{D}{kT}\int V_p(x)E(x)dx = \frac{D}{kT}\left[\int\left(\tilde{N}V_p + \tilde{N}V_0\right)dx\right] = \text{Constant} \quad \text{* MERGEFORMAT (57)}$$

where the integral in the second term of Equation * MERGEFORMAT (57) corresponds to the total number of all vacancies in the oxide, both charged and neutral. When defect chemistry is active, the gradient of the neutral vacancy density is no longer zero and increases to a finite steady-state value. Hence, the gradient of the single-charge vacancy density must correspondingly decrease to keep the RHS of Equation * MERGEFORMAT (57) constant. The vacancy species fluxes plotted in Figure 18 reflect this situation where we note that the sum of the single-charged vacancy drift and diffusion components equal the neutral vacancy diffusion current as required by Equation * MERGEFORMAT (54) and consequently Equation * MERGEFORMAT (57)

We also note that charge neutrality in the oxide region is maintained, on average, by requiring $\left[V_p\right] = \left[n\right]$. Thus, inspection of Figure 19 indicates that Equation * MERGEFORMAT (57) relaxes the requirement that the magnitudes of the electron drift and diffusion currents be equal, as was the case for no defect chemistry being active, due to the presence of the neutral vacancy gradient.

The strength of the defect chemistry reaction described by Equation * MERGEFORMAT (49) on the transport properties of the device is made clear by tabulating the ratios of electron current density for the case of defect chemistry being on to that of the case where defect chemistry is off (i.e., the ratio of the two values in each box of Table 2). These ratios are tabulated in Table 3 for the case of $E_f = 0.0\ \text{eV}$, and the corresponding values in Table 3 are plotted in Figure 20. For the first two rows of Table 3, $V_p/V_0 = 1$ and $V_p/V_0 = 10$ and as observed in Table 3 and Figure 20, the effect of defect chemistry is strongest for these ratios of the diffusion coefficients when the activation energy (defect level) is between about

0.10 - 0.16 eV below the conduction band When the defect level is deeper, the defect chemistry reaction of Equation * MERGEFORMAT (49) becomes negligible. Conversely, one may intuitively expect that the strength of the reaction would be strongest when the defect level is zero, i.e., at the same level as the conduction band. Hence, the presence of a peak at $E_r \approx -0.1\ \text{eV}$ $V_p/V_0 = 1$ for and the shift of the peak to $E_r \approx -0.16\ \text{eV}$ for $V_p/V_0 = 10$ may seem surprising. However, this behavior can be understood by examining the vacancy concentration profiles (not shown) for a few activation energies about the peak $E_r = 0.0\ \text{eV}, -0.1\text{eV}, -0.2\ \text{eV}$. As expected, for the case of $E_r = -0.2\ \text{eV}$, the limiting situation is approached whereby defect chemistry is not effective, as discussed earlier. Placing the defect level closer to the conduction band does indeed result in the neutral vacancy gradient increasing, which of course, increases the strength of defect chemistry. However when the defect level approaches a value of approximately $E_r = -0.1eV$, the corresponding increase of the single-charged vacancy gradient has also increased to such an extent that the increased diffusion of single charge vacancies toward the anode results in a reduction of the neutral vacancy gradient, which in turn reduces the efficacy of defect chemistry. As indicated also in Figure 20, this effect is more pronounced as the ratio of V_p/V_o increases because the positively charged vacancies are allowed to diffuse faster toward the anode. Furthermore, as the concentration of single charge vacancies consequently increases toward the anode, they capture the electrons in that region released by the neutral vacancies resulting in a decreased electron current flow. The results in Table 3 are qualitatively similar for lower bias voltages.

Table 3. Ratio of current densities for chemistry on/off.
Bias Voltage = 1.0V, E_f = 0.0eV for all cases.

E_r (eV)

(V_p / V_o) Diffusion coef. ratio	0.0	-0.1	-0.2	-0.3
10^0	1.4477	2.4183	1.4104	1.0152
10^1	1.0521	1.2934	1.3482	1.0152
10^2	1.0052	1.0363	1.0927	1.0182
10^3	1.0005	1.0039	1.0121	1.0193
10^4	1.0001	1.0004	1.0012	1.0013

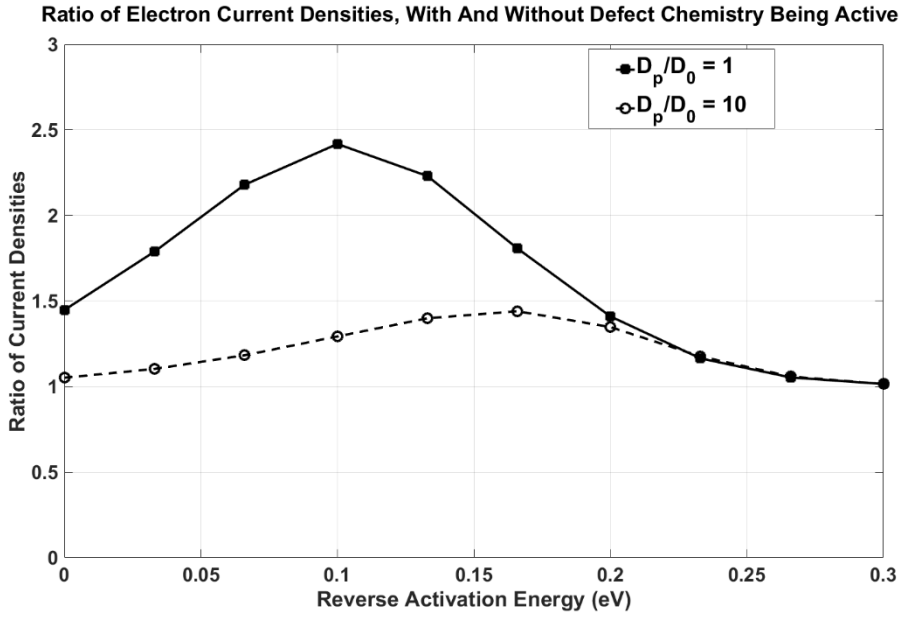

Figure 20. Ratios of electron current densities for defect chemistry being active or disabled for two ratios of diffusion coefficients.

4.4 Conclusion

A phenomenological model of M-I-M memristor operation has been presented in which electron transport through the device has been modeled using a variation of the well-known drift-diffusion formalism, wherein the effects of first-order defect chemistry for oxygen vacancies have been included. It has been shown that under a restricted set of operating conditions (certain

ratios of diffusion coefficients, low bias operation less than 1.0V for a 50nm thick oxide, constant lattice temperature) the values of electron current density through the device can vary upwards of about a factor of two as compared to the cases for which defect chemistry is not considered, over a range of shallow defect levels (approximately 0.1-0.15 eV) below the conduction band.

However, several of the parameter values used in the simulations, notably the values of the diffusion coefficients and the reaction cross-sections, are not known experimentally. Hence, the results may be considered inconclusive. It is intended though that this work serves as a guide for the development of a more complex, physics-based model of transport that is currently being developed by our research group for incorporation into the Sandia REOS and Charon codes. In this more advanced treatment of transport in oxide-based memristors, we also assume that electron transport in the oxide can be treated with the drift-diffusion formalism. However, this newer model is being extensively augmented by the inclusion of other bulk transport mechanisms, such as defect site hopping and Poole-Frenkel emission, and various tunneling mechanisms at the oxide/metal interfaces, such as band-to-defect tunneling and band-to-band tunneling between the electrodes and the oxide region.

5. SIMULATION OF BIPOLAR TANTALUM OXIDE MEMRISTOR

This section describes the simulation and validation of a bipolar tantalum oxide (TaOx) memristor. The fully-coupled thermo-electrical model has been applied to simulate the switching process in a 3D filamentary TaOx memristor shown in Figure 21. The layer material and thickness come from an experimental device published in Ref. [82]. Making use of the multi-physics capability in Charon, we solve the coupled Poisson, electron, oxygen vacancy, and heat equations in the active TaOx (which mimics the highly-conductive Ta electrode) and conduction filament (CF) regions, with vacancies confined in TaOx and CF regions, while in the Pt and Ta_2O_5 regions, due to absence of mobile vacancies, the coupled Poisson, electron, and heat equations are solved, with Pt treated as a highly doped n-type semiconductor using immobile dopants, and Ta_2O_5 as an undoped semiconductor. Holes are excluded here due to the n-type nature of TaOx memristors. The boundary condition for the temperature is set such that the topmost and bottommost surfaces of the device are fixed at 300 K as indicated in Figure 21, with the homogeneous Neumann condition applied to all other outer surfaces. Electrically, the very bottom of the device is grounded, and the voltage is applied at the top surface of the top Pt electrode. An Ohmic contact condition is assumed for electron density and electric potential at the topmost and bottommost surfaces of the device.

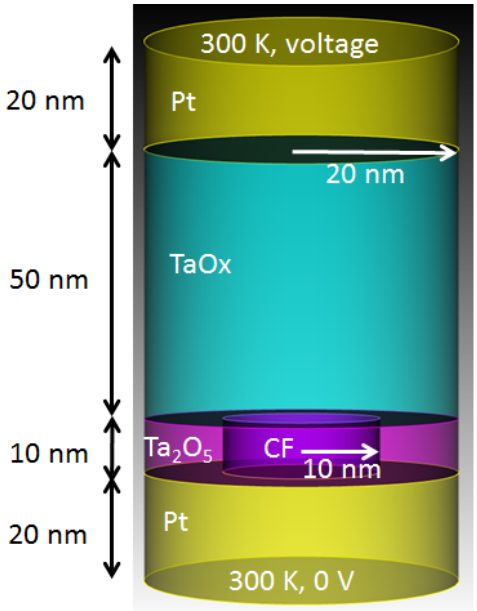

Figure 21. Simulated structure of a 3D filamentary TaOx memristor, with the layer material and thickness coming from an experimental device [84].

The experimental data from Ref. [84] indicate that this filamentary TaOx memristor shows bipolar switching behavior. In the following, we will apply our simulator to explore the bipolar RESET (i.e., OFF switching from low to high resistance state) and SET (i.e., ON switching from high to low resistance state) switching processes and the current-voltage hysteresis characteristics, and to compare simulation results with experimental data.

5.1 RESET Switching

We first explore the RESET switching. From Fig. 3(b) in Ref. [84], we observe that the measured device RESET resistance monotonically increases with time for a given voltage and with increasing negative voltage. To simulate how the device resistance changes during RESET and to provide insight and comparison with experimental data, we assume the device is in a conductive state after electroforming, by assigning mobile oxygen vacancies and electrons with a uniform density of $1x10^{21}$ cm^{-3} in the active TaOx and CF regions, and a uniform electron density of $1x10^{21}$ cm^{-3} in the Pt electrodes resulting from immobile n-type dopants. The initial temperature of the device is set to 300 K, and a negative DC (Direct Current) voltage is applied to the top Pt electrode.

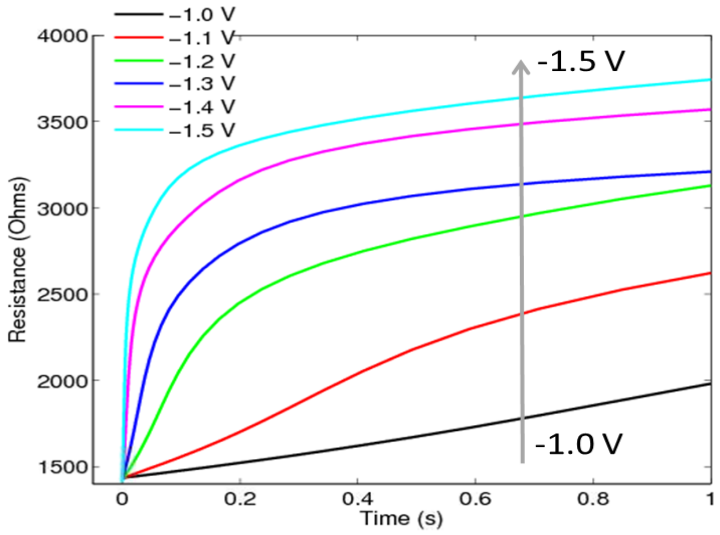

Figure 22. Simulated device resistance as a function of time under different voltage during RESET switching

Figure 22 plots the simulated device resistance as a function of time under different negative voltages during RESET switching. It is noted that the simulated resistance and time scale may appear quite different from the measured data [Fig. 3(b) in Ref. 84] since we have not done any calibration work yet. However, the variation profile of device resistance with time and voltage shows strikingly good agreement with experiment, which suggests that our fully-coupled model has captured the dominant RESET switching mechanism.

To investigate what happens in the device during RESET switching, we plot snapshots of carrier densities and temperature at different times with a -1.5V voltage applied at the top Pt electrode in Figure 23. Panels (a)-(d) correspond to the time of 0 s, 6.4558×10^{-10} s, 0.0011982 s, and 1 s respectively. In each panel, the bottom right figure shows the one-dimensional profiles of carrier densities and temperature along the z direction in the device center indicated by the white arrow in the bottom left figure; the values on the y axis of the bottom right figure need to be multiplied by 5×10^{20} cm^{-3} for carrier densities and by 300 K for temperature. Panel (a) shows the initial state where the active TaOx and CF regions have a uniform vacancy density of 10^{21} cm^{-3} (top left figure), the entire device except the insulating Ta_2O_5 region surrounding the CF has a uniform electron density of 10^{21} cm^{-3} (top right figure), and the device initial temperature is set to 300 K (bottom left figure). As -1.5V is applied to the top Pt electrode, the temperature increases on the order of hundreds of picoseconds due to Joule heating and the initial heating is broad in space, as shown in panel (b). Consequently, oxygen vacancies in the hottest spot near the TaOx/CF interface start to move around microseconds and move away from CF into TaOx under the influence of both heating and field. This process first leads to a vacancy and electron density gap in the CF as illustrated in panel (c). As time progresses, the density gap is further enlarged and eventually the entire CF is depleted of vacancies and electrons as shown in panel (d), leading to the RESET state. It is seen that as the CF becomes more resistive, Joule heating is more localized in the CF due to stronger electric field there, as demonstrated by the localized temperature profile in panel (d).

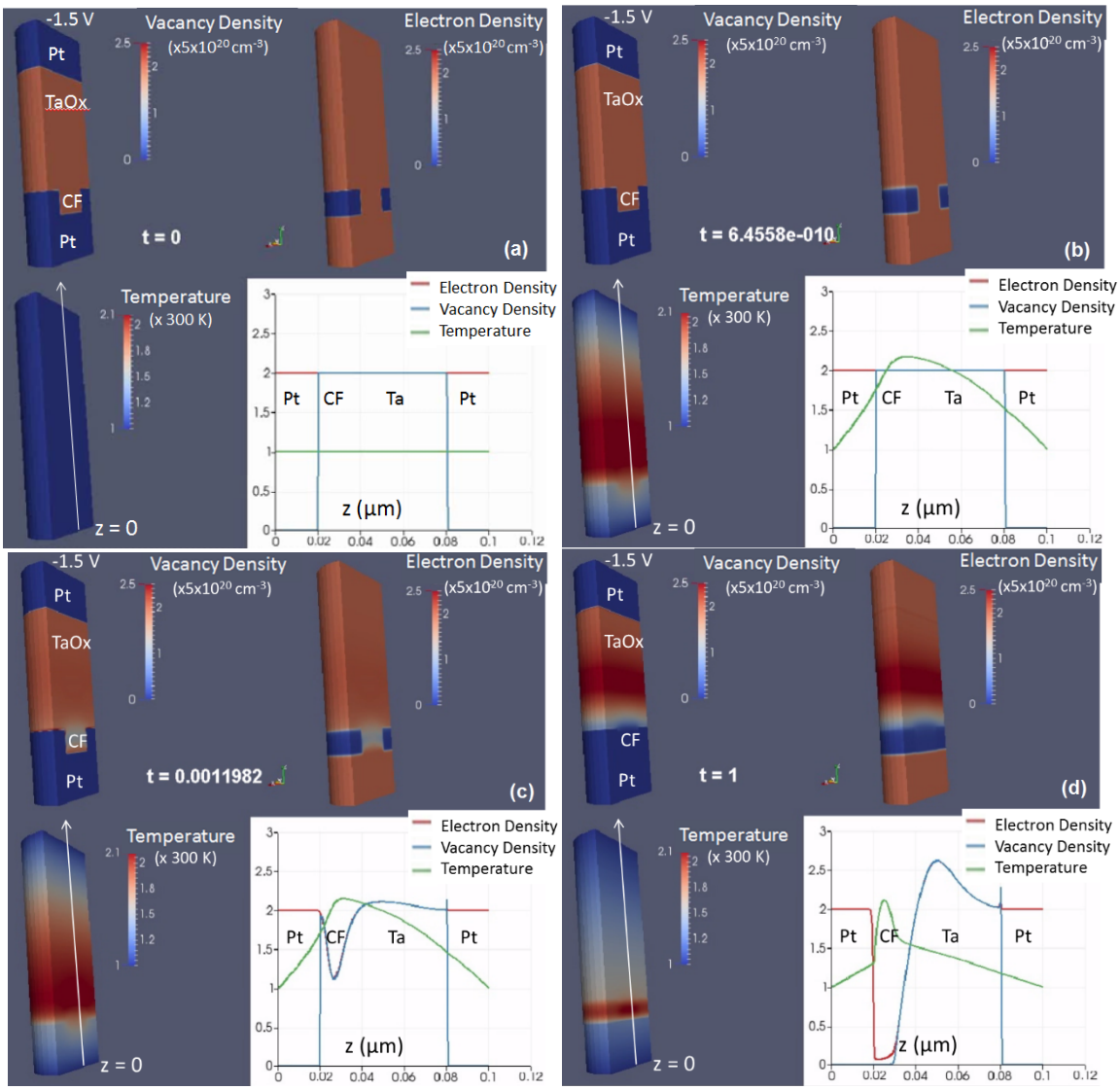

Figure 23. Snapshots of vacancy density, electron density, and temperature at different times with a -1.5 V voltage applied at the top Pt electrode.

From the simulation results, it is evident that the RESET switching is a thermally-activated field-dominant process: without Joule heating, oxygen vacancies would not move at all according to the RPI model, given the applied voltage and the geometry; only with Joule heating, the raised temperature enables the movement of vacancies, and the field drift component is much stronger than either the diffusion or the Soret component and hence dominates the overall motion of vacancies. Additionally, it is noted that the thermal transient dynamics occurs on a much shorter time scale than the electrical dynamics (e.g., hundreds of picoseconds compared to microseconds), which observation is strikingly consistent with other simple models [83,84].

Finally, it is worthy of noting that electrons in the active TaOx and CF regions closely follow the vacancies, suggesting that positively charged mobile oxygen vacancies indeed act as n-type dopants in n-type oxide memristors. This connection has been speculated by many authors in literature, but has not been shown explicitly.

5.2 SET Switching

Next, we explore the SET switching in the bipolar TaOx memristor. Figure 3(a) in Ref. [84] shows that the measured device SET resistance monotonically decreases with time for a given voltage and with increasing positive voltage. To simulate the changing of the device resistance with time and voltage during SET switching and to provide insight and comparison with experimental data, we assume the device begins in a RESET state and apply a positive voltage to the top Pt electrode. Figure 24 plots the simulated device resistance as a function of time under different positive voltages during SET switching. It is clear that the variation trend of the device resistance with time and voltage agrees reasonably well with experiment, even though the resistance values and time scale appear quite different from the measured data since we have not yet performed calibration.

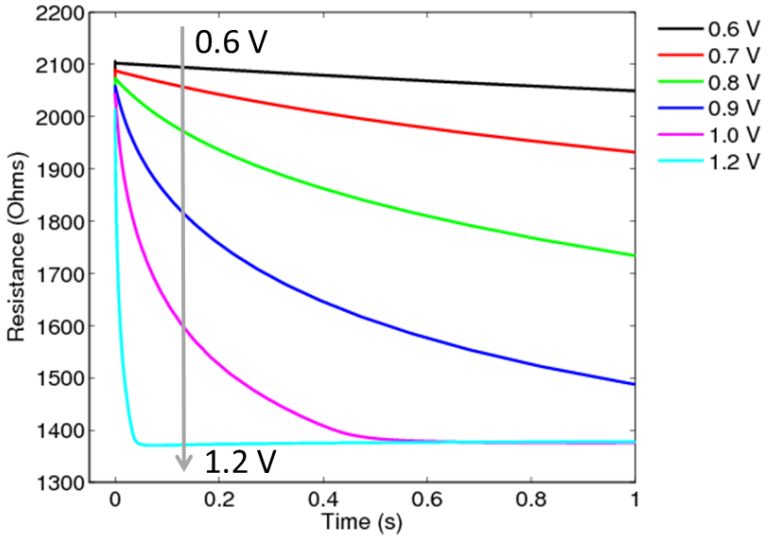

Figure 24. Simulated device resistance as a function of time under different positive voltages during SET switching.

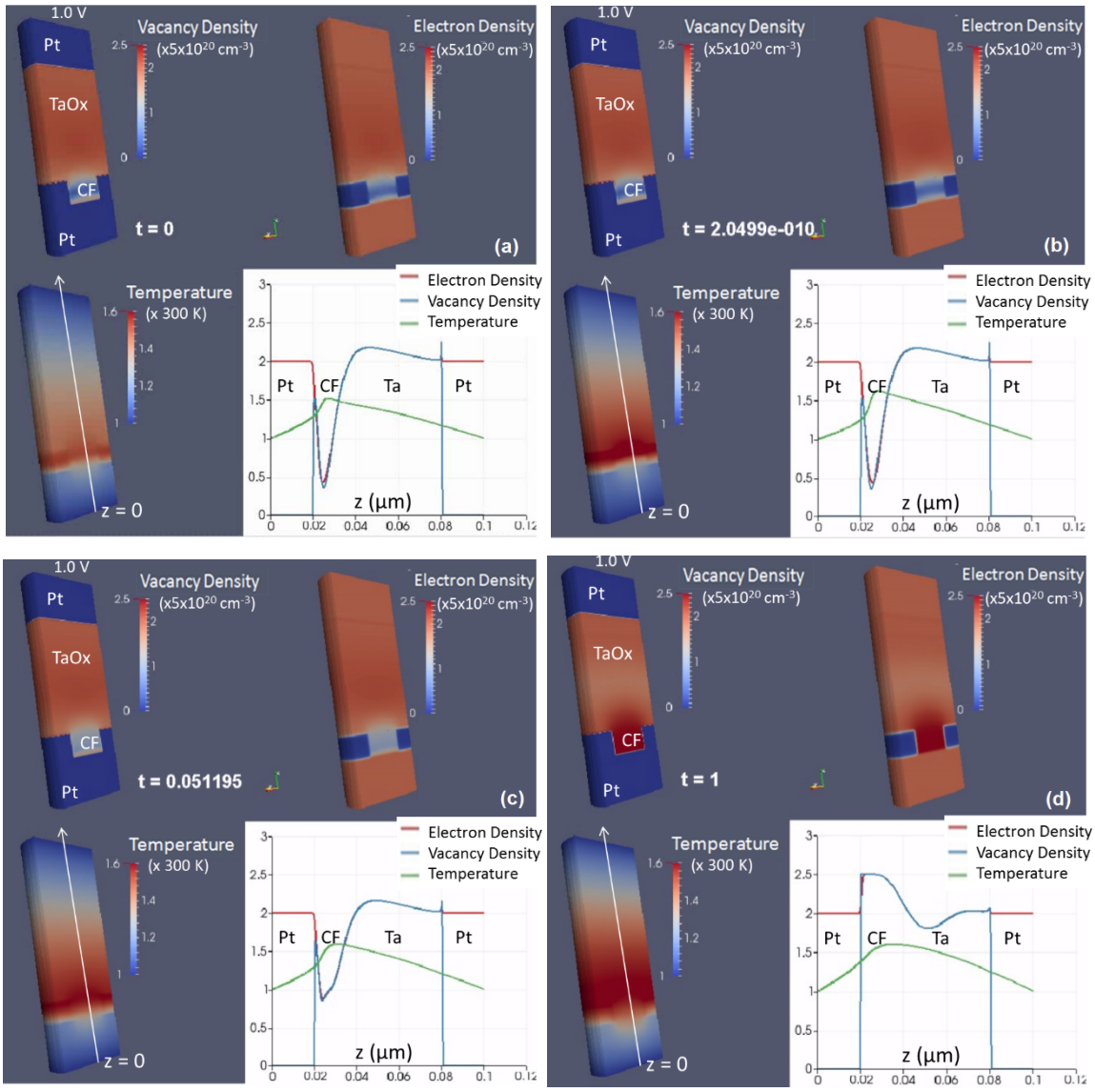

Figure 25. Snapshots of vacancy density, electron density, and temperature at different times with a 1 V voltage applied at the top Pt electrode.

To investigate what happens in the device during SET switching, Figure 25 plots snapshots of carrier densities and temperature at different times with a 1V voltage applied at the top Pt electrode. Panels (a)-(d) correspond to the time of 0 s, 2.0499×10^{-10} s, 0.051195 s, and 1 s respectively. Other notations are the same as Figure 23. Panel (a) shows that the device is initially in a RESET state resulted from a -1V voltage. As a positive 1V is applied to the device, Joule heating causes the temperature to have a moderate rise from the initial RESET state on the order of hundreds of picoseconds (similar to that of the RESET process), as shown in panel (b).

The rising temperature and applied electric field cause oxygen vacancies to move from the TaOx into the CF region to refill the density gap, as illustrated in panel (c). Once the density gap in the CF is fulfilled, vacancies continue moving from the TaOx into the CF due to the dominant driving of the electric field. In order to avoid unphysical pile-up of vacancies, the artificial diffusion model described in Section 2.2 was used to limit the maximum vacancy density to a somewhat arbitrary value of $1.25\text{x}10^{21}$ cm^{-3}. The choice of this value was based on the assumption that the CF should not be much more conductive than the TaOx region which mimics the Ta electrode in the experimental device. As shown in panel (d), the vacancy and electron densities in the CF are indeed limited to $2.5\text{x}5\text{x}10^{20} = 1.25\text{x}10^{21}$ cm^{-3}, where $5\text{x}10^{20}$ is a concentration scaling factor. It is interesting to note that the RESET switching in Section 4.1 does not need using the artificial diffusion model to limit the vacancy density, but it is a self-limiting process in which the maximum vacancy density is self-limited once the device is turned off. Finally, panel (d) shows that as the CF becomes more conductive, the heating is more spread out in space. It is clear that the SET switching is also a thermally-activated field-dominant process, similar to that of the RESET switching.

5.3 Current-Voltage Hysteresis

After simulating and identifying the main physical mechanism responsible for the bipolar RESET and SET switching processes, we applied the fully-coupled model to simulate the current-voltage hysteresis characteristics. To do this, triangular voltage sweeps with different sweeping rates are applied to the device as plotted in Figure 26 (a). The resulting current waveforms are plotted in Figure 26(b), and the corresponding current-voltage hysteresis curves are given in Figure 26(c). From Figure 26(a) and Figure 26(b), it is interesting to observe that the current waveforms nearly follow those of the voltages around the positive peaks, while they are significantly different from the voltage waveforms around the negative peaks. This observation is surprisingly consistent with the measured voltage and current waveforms shown in Fig. 4(a) of Ref. [84]. The simulated current-voltage curves in Figure 26(c) indicate that, for the smallest sweeping rate of 1 V/s, the device was never turned off during negative voltages due to insufficient heating, hence showing an Ohmic behavior, while for the higher sweeping rates of 1.5 V/s and 2 V/s, the hysteresis characteristics is clearly observed, because the device was indeed turned off during negative voltages and was able to turn on during positive voltages due

to sufficient heating. Comparing (c) with the measured current-voltage hysteresis in Fig. 2(b), Ref. [86], we see that the simulated shape for the 2 V/s case (green curve) is in very good agreement with experiment, even though the current and voltage values are different due to lack of calibration. The main noticeable difference in the shape is that, the simulated hysteresis shows an Ohmic behavior for voltages greater than 1 V, due to the imposed maximum vacancy density limit, while the Ohmic part is not shown in the measurement. However, it is interesting to note that the measured hysteresis shows asymmetry in the voltage range, e.g., the curve goes to -1 V but stops around 0.5 V, which makes it difficult to know if an Ohmic behavior may be possible in experiment at voltages greater than 0.5 V.

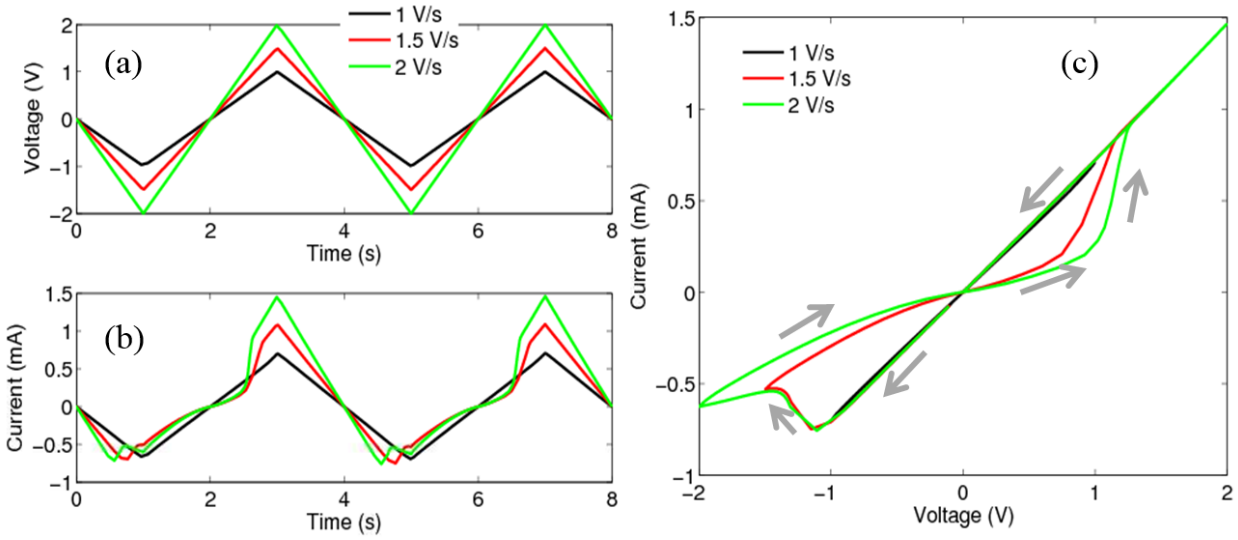

Figure 26. Current-voltage hysteresis characteristics: (a) triangular voltage sweeps with three different sweeping rates; (b) resulting current waveforms under the triangular voltage sweeps; (c) corresponding current-voltage hysteresis curves, where the gray arrows indicate the switching direction.

Before moving on to the next subsection, it is worthy of adding a note about the sign of the Soret coefficient S_V. Several research groups [85,86] argue that the Soret coefficient should be negative for vacancies, i.e., $S_V = - E_a / (k_B T^2)$, where E_a is an activation energy, implying that vacancies move from cold to hot regions. On the other hand, it is well-known (see e.g. Ref.[87]) that electrons in n-type semiconductors and holes in p-type semiconductors both move from hot to cold regions, i.e., $S_V = E_a / (k_B T^2)$, the Soret coefficient has a positive sign. However, the

nature of vacancy movement under temperature gradient is quite complicated, and it is debatable to state a single sign for the Soret coefficient. But for the bipolar switching, our simulations show that the sign of the Soret coefficient is not important, since the thermally-activated field drift component is much stronger than the diffusion and the Soret components, and the field drift dominates the switching process.

5.4 Comparison with Experiment and Parameter Calibration

In this section, we demonstrate that our MCT Simulator implemented in Charon TCAD enables us to calibrate simulation results with experimental data using the least number of parameters, and to perform parameter study for exploring device design space. Within experimentally measured set of values we optimized the fit to the calibration experiment. We then verified the calibrated parameters by simulating other devices and still obtained good agreement with experimental data. For calibration purpose, three parameters were varied while all other parameters were kept the same. The three parameters were the filament radius, the electron mobility, and the maximum vacancy density used in the artificial diffusion model. Figure 27 shows the comparison of current-voltage hysteresis between MCT simulation results and the experimental data in Ref. [84], where the simulations were done using a filament radius of 15 nm, an electron mobility of 40 $cm^2/(V.s)$, and a maximum vacancy density of 1.5×10^{21} cm^{-3}. It is seen that the simulation results agree quite well with the experiment just using the three parameters for calibration.

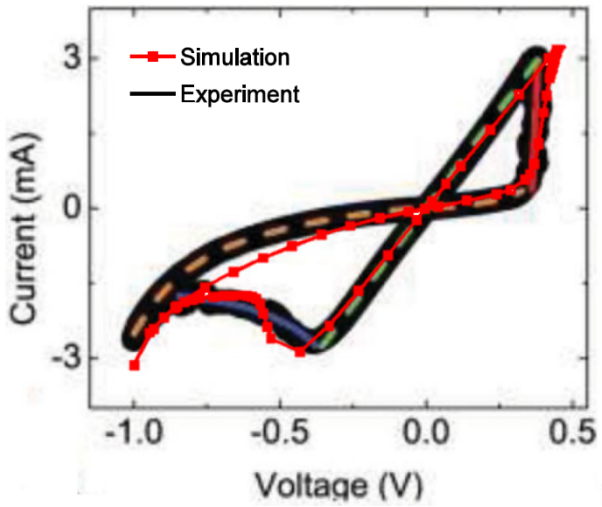

Figure 27. Current-voltage hysteresis comparison between simulation and experiment

Figure 28 shows the variation of the current-voltage hysteresis with selected parameters. Panel (a) shows the changing of the current-voltage hysteresis with the electron mobility, with the device radius set to 20 nm, the filament radius equal to 10 nm, and the maximum vacancy density being 1.25×10^{21} cm^{-3}. It is seen that a higher electron mobility leads to a higher current for a given voltage, which holds true in both the Ohmic and nonlinear regimes.

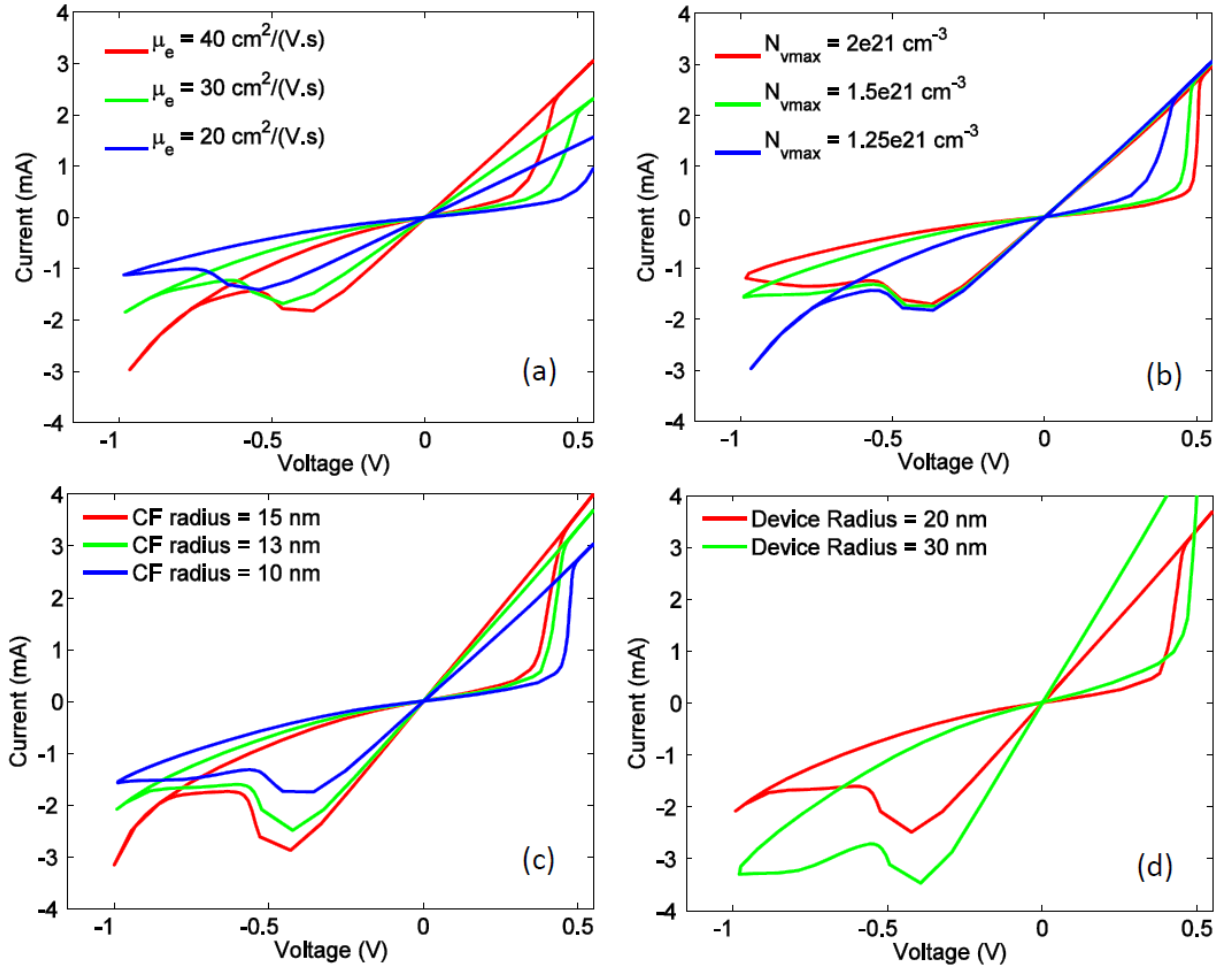

Figure 28. Variation of current-voltage hysteresis with selected parameters

Panel (b) shows the variation of the current-voltage hysteresis with the maximum vacancy density, while keeping the device radius at 20 nm, the filament radius at 10 nm, and the electron mobility at 40 cm^2 / (V.s). Interestingly, the value of the maximum vacancy density does not

affect the Ohmic behavior in the Ohmic regime, but has a significant effect on the current-voltage hysteresis in the nonlinear regime. During the RESET switching (i.e, the negative voltage regime), a smaller maximum vacancy density leads to a higher off-current and a nearly constant off-resistance at high voltages. This is because the imposed maximum vacancy density limit prevents the density gap from further depletion during RESET and consequently a higher off-current and a nearly constant off-resistance once the voltage reaches a critical value. Panel (c) shows the variation of the current-voltage hysteresis with the filament radius, while keeping the device radius at 20 nm, the electron mobility at 40 cm^2 / (V.s), and the maximum vacancy density at 1.5×10^{21} cm^{-3}. It is clear that a larger filament radius results in a higher current in both the Ohmic and nonlinear regimes. Panel (d) shows the variation of the current-voltage hysteresis with the device radius, while keeping the filament radius at 13 nm, the electron mobility at 40 cm^2 / (V.s), and the maximum vacancy density at 1.5×10^{21} cm^{-3}.

5.5 Conclusion

The generality of the fully-coupled thermo-electrical model allows us to simulate and investigate the underlying physical switching mechanisms in a wide spectrum of oxide memristors ranging from field-dominant, field-thermal-driven to thermal-dominant memristive devices. In this chapter, the model has been applied to simulate the RESET and SET switching processes in a 3D bipolar filamentary TaOx memristor. Extensive simulations show that the switching dynamics of the bipolar device is determined by thermally-activated field-dominant processes [88]. Specifically, (i) during RESET switching, when a sufficient negative voltage is applied to the top Pt electrode, Joule heating causes the increase of temperature with the hottest spot located in the CF, and consequently, oxygen vacancies move away from the CF into the TaOx electrode under the influence of both heating and field, which leads to a vacancy density gap and possible depletion of vacancies in the entire CF at high negative voltages, resulting in the RESET state; (ii) during SET switching, a sufficient positive voltage causes Joule heating and the increase of temperature, and subsequently, the rising temperature and electric field cause vacancies to move from the TaOx into the CF to refill the density gap, switching to the SET state. Simulated device resistance profiles as a function of time and voltage during RESET and SET switching show good agreement with experimental measurements [90]. Furthermore, the simulated current-voltage hysteresis shows a very good agreement with the measured result by calibrating only

three parameters [89]. A parameter study was also performed to investigate the effects of different parameters on the current-voltage hysteresis characteristics. The comprehensive simulator will greatly aid in the understanding of underlying switching physics in a large variety of oxide memristors, and it will facilitate the experimental development of memristive devices for post-CMOS memory and logic applications.

6. CONCLUSIONS

We have created a MCT Simulator that solves, simultaneously, the coupled differential equations: the time-dependent drift-diffusion equations for electrons, holes, and ions/vacancies; the time-dependent lattice heat equation; and the Poisson equation for all the charged species in three spatial dimensions. The drift-diffusion equation for each species includes field drift currents due to electric potential gradients, concentration gradients (Fickian diffusion), and temperature gradients (Soret effect). The heat equation contains Joule heating contributions from all the species. The Simulator will greatly aid Sandia experimentalists in device optimization for different applications. Our MCT Simulator

- helps to establish a clear physical picture of resistance switching in TMO memristors
- has been successfully validated on the existing experimental data and allows accurate prediction of bipolar TMO memristor electrical characteristics.

Simulation of complex switching phenomena in transition metal oxide materials required new computational approaches that were implemented in the continuum TCAD tool Charon that captures effects of

- many species transport
- changes in material composition
- thermophoresis
- self-heating

We performed identification and calibration of sophisticated physical models and materials parameters for TaOx devices, identified criteria of importance of chemical reactions in memristive switching, and studied numerous transport mechanisms in TaOx materials.

It is important to point out that the MCT Simulator can be extended to simulate other novel beyond-CMOS technologies such as phase-change devices, and ultra-scaled batteries (e.g. Li-ion). Particularly attracting is the possibility to augment the MCT Simulator with necessary tunneling physics to be able to simulate novel TB-ReRAM devices that are now being fabricated experimentally at Sandia. It is known that ReRAM exhibits large resistive-switching fluctuation and suffers from leakage current in cross-point array operation. Recently, it has been experimentally demonstrated that the selectivity and switching uniformity can be dramatically improved by designing the device with a triple-layer structure of a tunnel-barrier-layer-inserted ReRAM. The tunnel barrier acts as an internal resistor whose resistance changes with the applied

bias and, if properly designed, can significantly improve the switching uniformity. The extension of simulation capability to TB-ReRAM devices would greatly aid the corresponding experimental effort.

Overall, our MCT Simulator provides:

- Accurate predictive modeling
- Rapid design/prototyping cycles
- Fabrication validation and verification
- Extreme temperature analysis
- Efficient / low-cost technology development and maturation
- Data for architecture and algorithm development

Our continuum MCT Simulator aims at near-future aid to experimental memristor work. In order to perform a computational assessment of memristors' utility as potential replacement of CMOS logic and memory at the end of scaling (i.e. around 5nm feature size), a comprehensive investigation of the long-term scaling properties of memristive devices is necessary. As memristors are expected to scale into a few nanometer feature size in the future, such investigation will likely demand a particle-based (e.g. Monte Carlo) approach for ions/vacancies and a fully quantum-mechanical treatment (i.e. NEGF-based, see e.g. [90,91]) for electron and hole transport. In addition to exploring the new physics in ultra-small future memristors, the coupled Monte-Carlo-quantum transport based approach will become complementary to the continuum approach described in this work, providing higher fidelity verification for the continuum calculations.

7. REFERENCES

1. Proceedings of the IEEE (special issue)*: Memristors: Devices, Models, and Applications*, vol. 100, No. 6 (2012).
2. http://www.electronicsweekly.com/articles/06/10/2011/51988/ief2011-hp-to-replace-flash-and-ssd-in-2013.htm
3. U.S. Patent 7,203,789
4 M. Di Ventra *et al*, Proceedings of the IEEE 97, 171 (2009)
5. Kuk-Hwan Kim *et al*, Nano Lett. 12, 389−395 (2012).
6. D. Sacchetto, G. De Micheli, Y. Leblebici, Proceedings of the IEEE, 100, No. 6, pp. 2008-2020 (2012).
7. P. Meuffels · H. Schroeder, Appl. Phys. A 105, 65–67 (2011).
8. P. Meuffels, R. Soni, arXiv:1207.7319 (2012).
9. M. Di Ventra, M.; Y.V. Pershin, arXiv:1302.7063 (2013).
10. N. Hashem, S. Das, Applied Physics Letters 100, 262106 (2012).
11. L. O. Chua, IEEE Transactions on Circuits Theory **18**, 507 (1971).
12. G. Dearnaley, A. M. Stoneham, and D. V. Morgan, Reports on Progress in Physics **33**, 1129 (1970).
13. D. B. Strukov, G. S. Snider, D. R. Stewart, and R. S. Williams, Nature **453**, 80 (2008).
14. R. Waser (Ed.), *Nanoelectronics and Information Technology*, 3rd Edition, Wiley (2012).
15. D. S. Jeong *et al*, Reports on Progress in Physics **75**, 076502 (2012).
16. J. J. Yang, D. B. Strukov, and D. R. Stewart, Nature Nanotechnology **8**, 13 (2013).
17. D. H. Kwon *et al*, Nature Nanotechnology **5**, 148 (2010).
18. J. P. Strachan *et al*, Advanced Materials **22**, 3573 (2010).
19. F. Miao *et al*, Advanced Materials **23**, 5633 (2011).
20. S. H. Chang *et al*, Appl. Phys. Lett. **92**, 183507 (2008).
21. M. D. Picket *et al*, J. Appl. Phys. **106**, 074508 (2009).
22. J. Borghetti *et al*, J. Appl. Phys. **106**, 124504 (2009).
23. D. B. Strukov, J. L. Borghetti, and R. S. Williams, Small **9**, 1058 (2009).
24. A. S. Alexandrov *et al*, Appl. Phys. Lett. **99**, 202104 (2011).
25. D. B. Strukov and R. S. Williams, Appl. Phys. A **102**, 851 (2011).
26. J. P. Strachan *et al*, Nanotechnology **22**, 254015 (2011).
27. U. Russo, D. Ielmini, C. Cagli, and A. L. Lacaita, IEEE Trans Electron Devices **56**, 186 (2009).
28. S. Menzel *et al*, Advanced Functional Materials **21**, 4487 (2011).
29. D. B. Strukov, F. Alibart, and R. S. Williams, Appl. Phys. A **107**, 509 (2012).
30. X. Gao *et al*, presentation at the 2012 Trilinos User Group Meeting, October 2012.
31. X. Gao, E. Nielsen, R. P. Muller, R. W.Young, A. G. Salinger, N. C. Bishop, M. P. Lilly, and M. S. Carroll, *J. Appl. Phys.*, 114, 164302 (2013).
32. Synopsys Inc., *Taurus Medici User Guide*, Version Y-2006.06, June 2006.
33. M. Lundstrom, Fundamentals of Carrier Transport, p. 236, Cambridge University Press, Cambridge (2000).

34. D. B. Strukov, F. Alibart, and R. S. Williams, Appl. Phys. A, 107, 509 (2012).
35. S. P. Gaur and D. H. Navon, IEEE Trans. Electron Devices, ED-23(1), 50 (1976).
36. M. S. Adler, IEEE Trans. Electron Devices, ED-25(1), 16 (1978).
37. Chryssafis and W. Love, *Solid-State Electronics*, 22, 249 (1979).
38. G. K. Wachutka, *IEEE Trans. CAD*, 9(11), 1141 (1990).
39. U. Lindefelt, *J. Appl. Phys.* 75, 942 (1994).
40. J. E. Parrott, *IEEE Trans. Electron Devices*, 43(5), 809 (1996).
41. S. Kim, S. Choi, and W. Lu, *ACS Nano*, 8 (3), 2369 (2014).
42. D. B. Strukov and R. S. Williams, *Appl. Phys. A*, 94, 515 (2009).
43. N. Cabrera and N. F. Mott, *Rep. Prog. Phys.,* 12, 163 (1948).
44. J. D. Greenlee, J. C. Shank, M. B. Tellekamp, and W. A. Doolittle, *J. Appl. Phys.*, **114**, 034504 (2013).
45. A. N. Brooks and T. J. R. Hughes, Comput. Methods Appl. Mech. Engrg. 32(13), 199-259 (1982).
46. P. Bochev, M. Perego, and K. Peterson, SIAM J. Numer. Anal. 53(5), 2363–2388 (2015).
47. P. Bochev and K. Peterson, Cent. Eur. J. Math. 11(8), 1458-1477 (2013).
48. X. Gao, A. Huang, K. Peterson, G. Hennigan, L. Musson, and P. Bochev, "Implementation of different stabilization schemes in Charon using Trilinos/Panzer," presentation at Trilinos User Group Meeting, October 26-28, 2015, Albuquerque, NM.
49. http://trilinos.org
50. https://cubit.sandia.gov/
51. http://www.paraview.org/
52. N. D. Arora, J. R. Hauser, and D. J. Roulston, "Electron and Hole Mobilities in Silicon as a Function of Concentration and Temperature," *IEEE Transactions on Electron Devices*, vol. ED-29, no. 2, pp. 292-295 (1982).
53. D. J. Roulston, N. D. Arora, and S. G. Chamberlain, "Modeling and Measurement of Minority-Carrier Lifetime versus Doping in Diffused Layers of n+-p Silicon Diodes," *IEEE Transactions on Electron Devices*, vol. ED-29, no. 2, pp. 284-291 (1982).
54. C. J. Glassbrenner and G. A. Slack, "Thermal Conductivity of Silicon and Germanium from 3 K to the Melting Point," *Physical Review*, vol. 134, no. 4A, pp. A1058-A1069 (1964).
55. Atlas User's Manual (Device Simulation Software), www.silvaco.com, Oct. 2, 2013 edition.
56. D. B. Strukov, J. L. Borghetti, and R. S. Williams, "Coupled Ionic and Electronic Transport Model of Thin-Film Semiconductor Memristive Behavior," Small, vol. 5, no. 9, pp. 1058-1063, (2009).
57. "International Technology Roadmap for Semiconductors," in 2013 Edition, "Emerging research devices," [Online]. Available: www.itrs.net
58 . C. Chevallier, in *RRAM, presented at ITRS SCM Workshop* [Online]. Available: http://www.itrs.net/ITWG/ERD_files.html
59. Marinella, "The Future of Memory," in Proc. *IEEE Aerosp. Conf.*, Big Sky, MT, USA, 2013, pp. 1-11.
60. M.-J. Lee, C.B. Lee, D. Lee, S.R. Lee, M. Chang, and J.H. Hur et al., "A fast, high endurance and scalable non-volatile memory device made from asymmetric Ta_2O_{5-x}/TaO_{2-x} bilayer structures," *Nat. Mater.*, vol. 10, no. 8, pp. 625-630, Jul. 2011.
61. J.J. Yang, D.B. Strukov, and D.R. Stewart, "Memristive devices for computing," *Nat. Nano.*, vol. 8, no. 1, pp. 13-24, Jan. 2013.

62 . H. Akinaga and H. Shima, “Resistive random access memory (ReRAM) based on metal oxides,” in *Proc. IEEE,* Oct. 2010, vol. 98, no. 12, pp. 2237-2251.
63. F. Miao, J.P. Strachan, J.J. Yang, M.-X. Zhang, I. Goldfarb, and P.E. Torrezan *et al.*, “Sub Anatomy of a nanoscale conduction channel reveals the mechanism of a high-performance memristor,” *Adv. Mater.*, vol. 23, no. 47, pp. 5633-5640, Nov. 2011.
64 . A.C. Torrezan, S. J. Paul, M.-R. Gilberto, and R.S. Williams, “Sub-nanosecond switching of a tantalum oxide memristor,” *Nanotechnology*, vol. 22, no. 48, p. 485203, Dec. 2011.
65. M.J. Marinella, A.J. Lohn, J.E. Stevens, S. Deckler, P.R. Mickel, and D.R. Hughart *et al.*, “A CMOS compatible forming free TaO_x ReRAM” presented at the ECS Fall Meeting, San Francisco, CA, USA, 2013.
66. M.J. Marinella, S. M. Dalton, P. R. Mickel, P. E. Dodd, M. R. Shaneyfelt, E. Bielejec, G. Vizkelethy and P. G. Kotula, "Initial assessment of the effects of radiation on the electrical characteristics of TaO_x memristive memories," *IEEE Trans. Nucl. Sci.,* vol. 59, no. 6*,* pp. 2987-2994, 2012.
67. P.R. Mickel, A. J. Lohn, B. J. Choi, J. J. Yang, M.-X. Zhang, M. J. Marinella, C. D. James and R. S. Williams, “A physical model of switching dynamics in tantalum oxide memristive devices,” *Applied Physics Letters,* vol. 102, no. 22*,* pp. 223502-5, 2013.
68. D.R. Hughart, A. J. Lohn, P. R. Mickel, S. M. Dalton, P. E. Dodd, M. R. Shaneyfelt, A. I. Silva, E. Bielejec, G. Vizkelethy, M. T. Marshall, M. L. McLain and M. J. Marinella, "A comparison of the radiation response of TaO_x and TiO_2 memristors," *IEEE Trans. Nucl. Sci.,* vol. 60, no. 1*,* pp. 4512-4519, Dec. 2013.
69. M.L. McLain, H.P. Hjalmarson, T.J. Sheridan, P. R. Mickel, D. Hanson, K. McDonald, D.R. Hughart and M. J. Marinella, “The Susceptibility of TaO_x-Based Memristors to High Dose Rate Ionizing Radiation and Total Ionizing Dose, memristor,” *IEEE Trans. Nucl. Sci.,* vol. 61, no. 6*,* pp. 2997-3004, Dec. 2014.
70. M. McLain, D. Hughart, D.J. Hanson, and M. J. Marinella, “Effects of ionizing radiation on TaO_x-based memristive devices,” in *2014 IEEE Aerosp. Conf.,* Big Sky, MT, 2014, pp. 1-9
71. M. McLain, M. J. Marinella, “Overview of the radiation response of anion-based memristive devices,” in *2015 IEEE Aerosp. Conf. (to be published),* Big Sky, MT, 2015, pp. 1-9.
72. R.Waser, R. Dittmann, G. Staikov and K. Szot, "Redox-Based Resistive Switching Memories – Nanoionic Mechanisms, Prospects, and Challenges," *Advanced Materials,* vol. 21, no. 25-26*,* pp. 2632-2663, 2009.
73. M.T. Brumbach, P.R. Mickel, A.J. Lohn, A.J. Mirabal, M.A. Kalan, and J.E. Stevens *et al.*, “Evaluating tantalum oxide stoichiometry and oxidation states for optimal memristor performance,” *J. Vac. Sci. Technol. A*, vol. 32, no. 5, pp. 051403-051407, 2014.
74. A.J. Lohn, J.E. Stevens, P.R. Mickel, D.R. Hughart, and M.J. Marinella, “A CMOS compatible forming free TaO_x ReRAM,” *ECS Trans.,* vol. 58, no. 5*,* pp. 59-65, Aug. 2013.
75. D.B. Strukov, R.S. Williams, “Exponential ionic drift: fast switching and low volatility of thin-film memristors,” *Applied Phys. A,* vol. 94*,* pp. 515-519, 2009.
76. B.D. Tierney, H.P. Hjalmarson, M.L. McLain, D.R. Hughart, M.J. Marinella, D. Mamaluy, “Transport in Thin Film Oxides: From M-I-M Capacitors to TaO_x-based Memristors,” (To be Published), 2016.
77. H.P. Hjalmarson, R.L. Pease, and R.A.B. Devine, “Calculations of radiation dose-rate sensitivity of bipolar transistors,” *IEEE Trans. Nucl. Sci.,* vol. 55, no. 6*,* pp. 3009-3015, Dec.

2008.
78. S.M. Sze, *Physics of Semiconductor Devices 2nd ed.,* New York, NY, USA, John Wiley & Sons, 1981, pp. 84-85.
79. N.W. Ashcroft, N.D. Mermin, *Solid State Physics,* Belmont, CA, USA, Brooks/Cole Cengage Learning, 1976, pp. 572-577.
80. P. Kofstad, *Nonstoichiometry, Diffusion, and Electrical Conductivity in Binary Metal Oxides,* New York, NY, USA, John Wiley & Sons, 1972, pp. 15-21.
81. R.M. Fleming, D.V. Lang *et al.*, "Defect dominated charge transport in amorphous Ta_2O_5 thin films," *J. of Appl. Phys.,* vol. 61, no. 6, pp. 2997-3004, 2014.
82. P. R. Mickel, A. J. Lohn, B. J. Choi, J. J. Yang, M. X. Zhang, M. J. Marinella, C. D. James, and R. S. Williams, "A Physical Model of Switching Dynamics in Tantalum Oxide Memristive Devices," *Appl. Phys. Lett.*, **102**, 223502 (2013).
83. J. P. Strachan, A. C. Torrezan , G. Medeiros-Ribeiro , R. S. Williams, "Measuring the Switching Dynamics and Energy Efficiency of Tantalum Oxide Memristors," *Nanotech.*, **22**, 505402 (2011).
84. P. R. Mickel, A. J. Lohn, C. D. James, and M. J. Marinella, "Isothermal Switching and Detailed Filament Evolution in Memristive Systems," *Adv. Mater.*, **26**, 4486 (2014).
85. S. Kim, S. Choi, and W. Lu, "Comprehensive Physical Model of Dynamic Resitive Switching in Oxide Memristor," *ACS Nano*, **8** (3), 2369 (2014).
86. D. B. Strukov and R. S. Williams, Exponential Ionic Drift: Fast Switching and Low Volatility of Thin-Film Memristors," *Appl. Phys. A*, **94**, 515 (2009).
87. T. M. Tritt and M. A. Subramanian, "Thermoelectric Materials, Phenomena, and Applications: A Bird's Eye View," *MRS Bulletin*, **31**, 188 (2006).
88. X. Gao, D. Mamaluy, E. Cyr, M. Marinella "Comprehensive Assessment of Oxide Memristors as Post-CMOS Memory and Logic Devices", ECS Transactions 72, 49 (2016).
89. X. Gao, D. Mamaluy, M. Marinella, "Comprehensive Assessment of Oxide Memristors as Post-CMOS Memory and Logic Devices," *Invited Presentation,* ECS-229, San Diego, May 2016.
90. X. Gao, D. Mamaluy, E. Nielsen, R. Young, et al. "Efficient self-consistent quantum transport simulator for quantum devices", J. Appl. Phys. **115**, 133707(2014).
91. D. Mamaluy, X. Gao, "The Fundamental Downscaling Limit of Field-Effect Transistors," APL **106**, 193503 (2015).

DISTRIBUTION

1	MS0899	Technical Library	9536 (electronic copy)
1	MS0359	D. Chavez, LDRD Office	1911 (electronic copy)


Sandia National Laboratories